ESD-TDR-64-48

1

Solid State Research

1964

Lincoln Laboratory

MASSACHUSETTS INSTITUTE OF TECHNOLOGY

Lexington, Massachusetts

1

Solid State Research

1964

Issued 4 June 1964

Lincoln Laboratory

MASSACHUSETTS INSTITUTE OF TECHNOLOGY

Lexington, Massachusetts

INTRODUCTION

I. SOLID STATE DEVICE RESEARCH

A Fabry-Perot interferometer, in which the effective spacing between the plates has been varied about 7 mm (by varying the pressure of the gas in the interferometer), has been used to obtain more information concerning the linewidth and output stability of CW GaAs diode lasers at 4.2°K operation. By observing the intensity of the center fringe as a function of gas pressure, the linewidth has been determined to be less than the 0.016-Å resolution of the instrument. With the Fabry-Perot set for one-half maximum transmission, the stability of the laser was observed over a period of 5 minutes. The stability was excellent, particularly when compared to that of a commercial gas He-Ne laser.

The far-field pattern from CW InAs diode lasers at 4.2°K has been measured. The observed beam angle of 7° × 30° is consistent with coherent emission from a filament of 6 microns perpendicular to the junction, and of 26 microns in the plane of the junction. This filament size is of the same order as that reported for GaAs diode lasers. External quantum efficiencies as high as 11 percent have been measured for these diodes. External quantum efficiency has been further increased, by about a factor of two, by the application of a magnetic field of 4 kgauss perpendicular to the direction of current flow. The output spectrum from spontaneously emitting InAs diodes shows an additional peak 28 mev below the main emission peak corresponding to radiation associated with the emission of one longitudinal optical phonon. The spectrum also shows a knee about 60 mev below the main peak corresponding to radiation associated with the emission of two longitudinal optical phonons.

Studies of the intensity of the spontaneous radiation from InSb luminescent diodes and the linewidth of the radiation, both as a function of longitudinal magnetic field, have been correlated with the reduction of the threshold current for laser action in a magnetic field. The results are consistent with published theory that the threshold should be inversely proportional to the intensity of the spontaneous (inverted) line at the lasing wavelength. The magnetic field also causes a splitting of the spontaneous line, which can be explained on the basis of spin splitting of the lowest Landau level.

The attenuation of the injection luminescence from PbSe and PbTe diodes has been measured in sapphire, CaF_2, and LiF_2. From these results, the luminescence peaks can be placed between 6 and 7 microns for PbTe and 8 and 9 microns for PbSe.

The problem of designing high-power laser diodes with optimum power efficiency has been considered. The results indicate that it should be possible to achieve 1-kw (pulse) output with 50-percent efficiency in GaAs.

II. LASER RESEARCH

The Raman laser program has received additional emphasis, in view of possible applications to high-power laser technology. Experiments have been set up to observe off-axis and right-angle, stimulated Raman emission. A large number of up- and down-shifted stimulated output lines have been obtained from a variety of organic liquids. On the theoretical side, the parametric interaction between stimulated Stokes and anti-Stokes radiation has been analyzed.

Spectral narrowing of the emission line has been observed in GaAs when optically pumped by a ruby laser.

An explicit quantum-mechanical expression for the photon detector correlation function has been derived.

Data concerning spectral and spatial properties of a laser-induced spark in air have been obtained.

Giant-pulse and conventional laser properties of Nd-doped glass have been examined. Wavelength and polarization data have been obtained for neodymium in several different host crystals.

Experiments are under way to observe magnetic-field-induced second-harmonic generation.

III. MATERIALS RESEARCH

The apparatus for growing refractory crystals with the induction plasma torch has been improved in several ways. Modification includes replacement of the quartz powder feed tube by a water-cooled stainless-steel tube extending through the hottest part of the plasma to within about an inch of the growing crystal. The modified apparatus is being used to grow crystals of the divalent oxides of the transition metals between titanium and nickel. In initial experiments, single crystals of MnO and CoO and large-grained boules of NiO have been prepared.

An oxide of chromium with spinel structure (a_0 = 8.379 Å) has been prepared by arc-melting equimolar quantities of chromium and Cr_2O_3 under argon. No structure of this type has been previously reported for any chromium oxide. Since Fe_3O_4 has a spinel structure with nearly the same lattice constant, it is likely that the new material is closer in composition to Cr_3O_4 than to CrO.

Samples with nominal compositions of $CrO_{1.87}$ and $CrO_{1.94}$ have been prepared by reacting CrO_3 and Cr_2O_3 in suitable proportions under high pressure. The Seebeck coefficients and resistivities of these samples are quite similar to those of CrO_2 prepared in the same manner.

The pressure dependence of the temperature at which α-Ag_2Se is transformed into β-Ag_2Se has been determined by measurements of resistivity vs temperature at various pressures. The transition temperature increases with pressure from 130°C at 1 atm to 300°C at 47 kbar. This is consistent with crystallographic evidence that β-Ag_2Se is the less dense form.

The temperature dependence of the rate at which cubic $PrO_{1.5}$ is transformed into the stable hexagonal form has been investigated. Samples of the cubic phase were prepared under conditions designed to exclude residual gases, annealed at elevated temperatures, quenched, and examined by x-ray diffraction. Only a small fraction of the material had transformed after heating for 96 hours at temperatures up to 775°C; most of it had transformed after only 6 minutes at 825° to 860°C.

Preliminary results indicate that In_4SbTe_3 prepared at high pressure exhibits superconductivity below 1.5°K. Samples prepared at atmospheric pressure, either by freezing from the melt or by annealing pressed powders, failed to become superconducting down to 1.3°K. The discrepancy is probably due to differences in composition. Investigation of the pseudo-binary InSb-InTe system by thermal analysis shows that In_4SbTe_3 is a peritectic compound that probably undergoes a solid-state transformation at about 420°C.

Partial pressures of $Te_2(g)$ and $GeTe(g)$ in equilibrium with condensed phases in the Ge-Te system have been determined as a function of temperature, by measuring the optical density of the vapor. The value of p_{Te_2} over $Ge_xTe_{1-x}(c)$ depends strongly on the composition of the solid phase, but p_{GeTe} is independent of this composition within the limits of experimental error. Values of the standard Gibbs free energy for the dissociation of $GeTe(g)$ into $Ge(g)$ and $Te_2(g)$ have been obtained from the partial-pressure data for Te-saturated Ge(c).

Analytical methods have been developed for determining chromium in chromium oxides and Al_2O_3 (ruby) by oxidizing the chromium to the +6 state with ammonium persulfate and then titrating it with ferrous ammonium sulfate. The titration end points in the chromium oxide and Al_2O_3 analyses are found by potentiometric and amperometric techniques, respectively. Methods based on EDTA titrations have been developed for determining magnesium and titanium in $MgTiO_3$ and nickel in NiO.

The technique described earlier for mass spectrographic analysis of insulating materials, in which electrodes are prepared by pressing a powdered mixture of the sample and a conductor, is being investigated further. Preliminary data indicate that better results can be obtained if graphite, the conducting powder originally used for electrodes, is replaced by silver of sufficient purity.

IV. BAND STRUCTURE AND SPECTROSCOPY OF SOLIDS

A new, more general equation has been proposed for the dispersion relation for electrons in bismuth. It is pointed out that the models currently used involve unjustified assumptions regarding the interactions which can be neglected.

Magnetoreflection studies of antimony have been initiated. The observed magnetoplasma effects in this semimetal cannot be accounted for on the basis of the three, tilted, ellipsoidal conduction bands alone.

Diagrammatic methods for the interpretation of magneto-optical data have been developed. Experiments involving free-charge carriers in a magnetic field can be analyzed by tracing a path on a diagram showing the behavior of the index of refraction.

In the studies of HgSe it has been confirmed that the conduction band is non-parabolic, and that the primary scattering mechanism for electrons is polar scattering by optical phonons. Excellent agreement between experiment and calculation has been achieved for transport phenomena in this material.

The theory of magnetic resonance saturation in crystals is being investigated. Difficulties in previously published work are pointed out. Effects such as the time evolution of a magnetic resonance system and its approach to a steady state have been investigated, and a paper on this work will be submitted for publication. More work is needed in this area, since the experimental results are not in agreement with any known theory.

In agreement with theory, it has been shown that the addition of impurities to bismuth reduces the Nernst coefficient but does not change the sign. The prediction has been verified for both n- and p-type impurities in various amounts. For example, the addition of 0.05 atomic percent of lead reduces the Nernst coefficient by a factor of five. The magnitude of the effect varies with the amount of the impurity as well as with the particular type of impurity.

V. MAGNETISM AND RESONANCE

The Landau-Lifshitz symmetry arguments for second-order phase transitions have been applied to the special case of Heisenberg exchange in the molecular-field approximation. It is shown that this method has the same region of validity, and gives results identical to those obtained by Bertaut's method of calculating spin configurations just below a transition temperature. Unlike Bertaut's method, however, it does not require a specific form for the exchange energy. The usefulness of this approach is illustrated by applying it to several materials, including β-MnS and α-Fe_2O_3.

Spin resonance has been observed in the cubic spinel $Co[Cr_2]O_4$ in the frequency range 24 to 125 kMcps from 4.2°K to the Curie temperature of ~100°K. Two types of resonance have been observed: one, a uniform mode accompanied by a number of satellites; and another, which has been identified tentatively as a kind of exchange resonance. The resonance behavior seems to be different in three different regions of temperature. A Heisenberg Hamiltonian in the molecular field approximation shows that the spins order first in a Néel configuration going down in temperature. This is followed by a region of complex spiral ordering which persists to low temperatures. However, neutron diffraction shows that the transverse-spin correlation does not appear just below the Néel spiral ordering temperature (though the z-component moments do follow the molecular field predictions). At low temperatures, the neutron diffraction results show transverse spin correlation. The three temperature regions in the spin-resonance data seem to be related to those of the neutron diffraction observations.

Work on the MnAs-MnSb and MnAs-MnP systems has continued. Procedures for chemical analysis have been worked out, a magnetometer sensitive to magnetic-moment variations of ~0.01 percent of the saturation value of nickel has been checked out, and much of the x-ray

work has been completed. The data continue to support our hypothesis of partial spin quenching in MnAs and total spin quenching in $\text{MnAs}_{1-x}\text{P}_x$ (if $x > 0.04$).

The Jahn-Teller ions Mn^{3+} and Cu^{2+} are known to be important because of spontaneous BH-loop squareness in ferrite memory cores. Direct observation of clustering, which would produce magnetic inhomogeneities, has never been found. However, we have now obtained indirect evidence for such clustering by observing that Mn^{3+} is unique in its ability to destroy ionic order in spirals where one-fourth of the octahedral sites are occupied by Li^+ and the other octahedral sites are occupied by M^{3+} or M^{4+}.

Electrolytic reduction and the construction of a low-temperature x-ray unit have produced significant results in our program of vanadite crystal growth.

Much improvement, due primarily to the employment of a pulse integrating technique, has been obtained in the signal-to-noise ratio of 70-kMcps phonon echoes in quartz. This has permitted a more accurate determination of the temperature dependence of the attenuation.

TABLE OF CONTENTS

REPORTS BY AUTHORS
ENGAGED IN SOLID STATE RESEARCH

15 January through 15 April 1964

PUBLISHED REPORTS

Technical Reports

TR No.				DDC and Hayden Nos.
320	Growing Helical Density Waves in Semiconductor Plasmas	C.E. Hurwitz	17 October 1963	DDC 432393
345	Interpretation of the Magnetic and Crystallographic Properties of Compounds with the B31 Structure	J.B. Goodenough	28 January 1964	DDC*

Group Report

No.				
1964-10	A High-Performance He^3 Refrigerator	C.J. Rauch	29 January 1964	DDC 433544 H-570

Journal Articles[†]

JA No.			
2025	Adaptation of Lattice Liquid Model to Gas Adsorption Phenomena	J.M. Honig W.H. Kleiner	Surface Science $\underline{1}$, 71 (1964)
2117A	Electron Ordering Transitions in Several Chromium Spinel Systems	R.J. Arnott A. Wold D.B. Rogers	J. Phys. Chem. Solids $\underline{25}$, 161 (1964)
2179	Magnetic Susceptibility of Praseodymium Oxides	S. Kern	J. Chem. Phys. $\underline{40}$, 208 (1964)
2190A	Theory of the Infinite Stage Nernst-Ettingshausen Refrigerator	T.C. Harman	Advanced Energy Conversion $\underline{3}$, 667 (1963)
2193	Theory of the Faraday Effect in Solids	L.M. Roth	Phys. Rev. $\underline{133}$, A542 (1964)

---

* Not yet assigned.

† Reprints available.

JA No.

2202	High Pressure Transition in InSb	R.E. Hanneman M.D. Banus H.C. Gatos	J. Phys. Chem. Solids 25, 293 (1964)
2214	Jahn-Teller Distortions Induced by Tetrahedral-Site Fe^{2+} Ions	J.B. Goodenough	J. Phys. Chem. Solids 25, 151 (1964)
2219	Preparation and Properties of Sodium and Potassium Molybdenum Bronze Crystals	A. Wold W. Kunnmann R.J. Arnott A. Ferretti	Inorg. Chem. 3, 545 (1964)
2223	Helium Temperature Ultraviolet Reflectometer for Use with Modified Spectrograph	W.J. Scouler	Appl. Optics 3, 341 (1964)
2224	Current Regulator for Ultraviolet Light Source	W.J. Scouler E.D. Mills	Rev. Sci. Instr. 35, 489 (1964)
2225	Reflectivity of HgSe and HgTe from 4 to 12 eV at 12 and 300°K	W.J. Scouler G.B. Wright	Phys. Rev. 133, A736 (1964)
2227	Internal Second-Harmonic Generation in Gallium Arsenide Lasers	L.D. Malmstrom J.J. Schlickman R.H. Kingston	J. Appl. Phys. 35, 248 (1964)
2238	The Dependence of the Upper Critical Field of Niobium on Temperature and Resistivity	E.S. Rosenblum S.H. Autler K.H. Gooen[*]	Revs. Modern Phys. 36, 77 (1964)
2241A	Ceramic Double Cell for Crystal Growth by Fused Salt Electrolysis	W. Kunnmann A. Ferretti	Rev. Sci. Instr. 35, 465 (1964)
2254	Refined Treatment of the Theory Pertaining to Operating Characteristics of Anisotropic Nernst-Ettingshausen Devices	J.M. Honig B.M. Tarmy	J. Appl. Phys. 35, 722 (1964)
2260	Bulk Solution of Ginzburg-Landau Equations for Type II Superconductor: Upper Critical Field Region	W.H. Kleiner L.M. Roth S.H. Autler	Phys. Rev. 133, A1226 (1964)
2275	High-Pressure Phase Transition in Tin Telluride	J.A. Kafalas A.N. Mariano	Science 143, 952 (1964)
2276	Ultrasonic Measurements in Normal and Superconducting Niobium	R. Weber	Phys. Rev. 133, A1487 (1964)

---

[*] Author not at Lincoln Laboratory.

JA No.

2277	Theory of Spin Resonance and Relaxation	P. N. Argyres P. L. Kelley	Phys. Rev. <u>134</u>, A98 (1964)
2282	Cascade Capture of Electrons by Ionized Impurities	D. R. Hamann A. L. McWhorter	Phys. Rev. <u>134</u>, A250 (1964)
2294	Semiconductor Lasers	T. M. Quist	Intl. Science and Technology, No. 26, 80 (1964)
2302	Injection Luminescent Pumping of $CaF_2:U^{3+}$ with GaAs Diode Lasers	R. J. Keyes T. M. Quist	Appl. Phys. Letters <u>4</u>, 50 (1964)
2306	Interferometric Phase Shift Technique for Measuring Short Fluorescent Lifetimes	R. J. Carbone* P. R. Longaker	Appl. Phys. Letters <u>4</u>, 32 (1964)
2312	A Theory of Thermoluminescence of Fluorite ($CaF_2:Y$). Radiative Recombination from Highly Associated Electron-Hole Pairs	J. R. O'Connor	Appl. Phys. Letters <u>4</u>, 126 (1964)
2326	Oriented Single-Crystal Bismuth Nernst-Ettingshausen Refrigerators	T. C. Harman J. M. Honig S. Fischler A. E. Paladino M. J. Button	Appl. Phys. Letters <u>4</u>, 77 (1964)
2328	Evidence That SnTe Is a Semiconductor	J. A. Kafalas R. F. Brebrick A. J. Strauss	Appl. Phys. Letters <u>4</u>, 93 (1964)

MS No.

895	Rapid Freeze Method for Growth of Bismuth Single Crystals	S. Fischler	Trans. Metallurgical Soc., AIME (March 1964) (Conference on Semiconductor Materials, Boston, 26-28 August 1963)
941	Spin Correlations Among Narrow-Band Electrons	J. B. Goodenough	J. Appl. Phys. <u>35</u>, 1083 (1964)
943	Electrical Conductivity in the Spinel System $Co_{1-x}Li_xV_2O_4$	D. B. Rogers J. B. Goodenough A. Wold	J. Appl. Phys. <u>35</u>, 1069 (1964)

---

* Division 4.

Journal Articles

JA No.

2268	Galvanomagnetic Effects in n-Type Germanium	W. E. Krag M. C. Brown	Accepted by Phys. Rev.
2270	Partial Pressures in Equilibrium with Group IV Tellurides. I. Optical Absorption Method and Results for PbTe	R. F. Brebrick A. J. Strauss	Accepted by J. Chem. Phys.
2295	Interface-Alloy Epitaxial Heterojunctions	R. H. Rediker S. Stopek J. H. R. Ward	Accepted by Solid-State Electronics
2296	Growth of $(Ga_xIn_{1-x})As$ Single Crystals by Vapor Phase Reaction	R. C. Sirrine	Accepted by J. Electrochem. Soc.
2307	Impurity States in Semiconducting Masers	H. J. Zeiger	Accepted by J. Appl. Phys.
2359	Acoustic Plasma Waves in Semi-metals	A. L. McWhorter W. G. May	Accepted by IBM J. Research Develop.
MS-968	The Fermi Surface of Graphite	M. S. Dresselhaus J. G. Mavroides	Accepted by IBM J. Research Develop. (Topical Conference on Semimetals, Columbia University, January 1964)

Meeting Speeches[*]

MS No.

589A	Superconducting Behavior of Some β-Tungsten Structure Niobium Compounds and Their Alloys	T. B. Reed H. C. Gatos W. J. LaFleur J. T. Roddy	Chemical Society, Tufts University, 11 March 1964
936A	The $CaWO_4/Nd^{3+}(Na^+)$ Optical Maser: Wavelength and Polarization Dependence on Resonator Geometry	D. F. Edwards	Physics Colloquium, University of Toledo, 4 March 1964
946	Effects of High Pressure-High Temperature Treatment on the Properties of Electronic Materials	E. P. Warekois	1964 International Conference on Materials, ASTM, Philadelphia, 3-6 February 1964
1045	Discussion of Paper "Preparation of New Materials and Structures by High Pressure Treatment"	M. D. Banus	

---

[*] Titles of Meeting Speeches are listed for information only. No copies are available for distribution.

MS No.

971	The Polarographic Determination of Mercury, Tellurium, and Cadmium in HgTe-CdTe Alloys	M.C. Gardels J.C. Cornwell	
972	Analysis of Vanadium-Gallium Alloys Based on the Displacement of Quinquevalent Vanadium from Its EDTA Complex	M.C. Gardels	Conference on Analytical Chemistry and Applied Spectroscopy, Pittsburgh, 2-6 March 1964
981A	Galvano-Thermomagnetic Phenomena in Bismuth	J.M. Honig T.C. Harman B.M. Tarmy	
990A	The Theory of Stimulated Raman Emission	H.J. Zeiger P.L. Kelley H.A. Haus*	
992	Properties of n- and p-Type PbSe with High Carrier Concentrations	A.J. Strauss	American Physical Society, New York, 22-25 January 1964
994	Bulk Solution of Ginzburg-Landau Equations for Type II Superconductor: Upper Critical Field Region	W.H. Kleiner L.M. Roth S.H. Autler	
992A	Some Electrical and Optical Properties of Semiconducting PbSe	A.J. Strauss	Graduate Seminar, Lowell Technological Institute, 11 March 1964
993	Acoustic Plasma Waves in Semimetals	W.G. May A.L. McWhorter	Topical Conference on Semimetals, Columbia University, 21 January 1964
985B	Experiments on Room Temperature Nernst-Ettingshausen Refrigerators	T.C. Harman J.M. Honig S. Fischler A.E. Paladino M.J. Button	
1020	Theory of Spin Resonance and Relaxation	P.N. Argyres P.L. Kelley	American Physical Society, Philadelphia, 23-26 March 1964
1021	Quantum Theory of Photo-Detection Statistics	P.L. Kelley W.H. Kleiner	
1023	Higher Order Corrections to the Molecular Field Theory of the Magnetic State	G.F. Dresselhaus	

---

* Author not at Lincoln Laboratory.

MS No.

1026	Partial Pressures in Equilibrium with Group IV Tellurides. III. GeTe	R.F. Brebrick A.J. Strauss	
1030	InAs Laser Characteristics	I. Melngailis	
1031	InSb Diode Laser Threshold Reduction with a Magnetic Field	R.J. Phelan R.H. Rediker	American Physical Society, Philadelphia, 23-26 March 1964
1036A	Magnetoreflection Experiments in Pyrolytic Graphite	M.S. Dresselhaus	
1093	Stimulated Raman Processes	H.J. Zeiger	
1008A	Injection Lasers	R.H. Rediker	IEEE, PTGED, Philadelphia, 22 January 1964
1016	Comments on the Lincoln Laboratory Far Infrared Program	D.H. Dickey	Symposium on Far Infrared Physics, Corona, California, 20-21 January 1964
1039	High Magnetic Field Far Infrared Radiation Sources	B. Lax D.T. Stevenson	
1027	Partial Pressures of $Te_2(g)$ and $MTe(g)$ Along the Three Phase Lines of $M_{1-x}Te_x(c)$ (M^2 = Ge, Sn, Pb)	R.F. Brebrick A.J. Strauss	Argonne National Laboratory, Argonne, Illinois, 26-27 February 1964
1028	Properties of n- and p-Type PbSe	A.J. Strauss	
1038	Injection Lasers	A.L. McWhorter	Cornell University, 17 March 1964
1041	Primarily Ionic Compounds with Metallic Conductivity	J.B. Goodenough	Naval Research Laboratory Seminar, Washington, 20 January 1964
1073	The First-Order Phase Change in MnAs	J.B. Goodenough	IBM Research Laboratory, Yorktown Heights, New York, 10 March 1964
1074	Multiple-Pumped Raman Laser	P.E. Tannenwald H.J. Zeiger	High Power Laser Technology, Redstone Arsenal, Huntsville, Alabama, 7-8 April 1964
1076	Injection Luminescent Pumping of $CaF_2:U^{3+}$	R.J. Keyes T.M. Quist	
1075	Injection Masers	R.H. Rediker	Industrial Liaison Symposium, M.I.T., 8 April 1964
1084	Image Tubes and Their Use in Re-entry Measurements	F.L. McNamara	IDA Discrimination Panel, Washington, 6 March 1964
1102	Applications of Order-Disorder Theory in the Study of Gas Adsorption Processes	J.M. Honig	Seminar, Union Carbide Corporation, Tarrytown, New York, 13 April 1964

ORGANIZATION

SOLID STATE DIVISION

A. L. McWhorter, *Acting Head*
P. E. Tannenwald, *Assistant Head*
M. J. Hudson, *Assistant*
D. T. Stevenson*

GROUP 81
SEMICONDUCTOR PHYSICS

J. M. Honig, *Leader*
T. C. Harman, *Assistant Leader*

Argyres, P. N.	Kelley, P. L.
Brebrick, R. F.	Kleiner, W. H.
Chapin, D. S.	Mason, V. J.
Dresselhaus, G. F.	Paladino, A. E.
Duston, D. K.†	Rawson, N. B.*
Gottschalk, M.	Sillers, S. J.
Hilsenrath, S.	Work, C. C.
Houghton, B. H.*	

GROUP 82
MAGNETISM AND RESONANCE

J. B. Goodenough, *Leader*
H. J. Zeiger, *Associate Leader*

Arnott, R. J.	Larson, E. G.*
Bermon, S.	Menyuk, N.
Delaney, E. J.	Newman, W. A.
Dwight, K., Jr.	Perry, F. H.
Feldman, B.	Ridgley, D. H.
Ferretti, A.	Rogers, D. B.
Germann, R. W.	Stickler, J. J.
Kaplan, T. A.	Thaxter, J. B.
Kern, S.	Weber, R.
Kernan, W. C.	Whipple, E. R.

GROUP 83
ELECTRONIC MATERIALS

E. P. Warekois, *Leader*
A. J. Strauss, *Assistant Leader*

Andrews, H. I.†	Gardels, M. C.
Bachner, F. J.†	Giardino, N. A.
Banus, M. D.	Kafalas, J. A.
Button, M. J.	LaFleur, W. J.
Carter, F. B.	Lavine, M. C.*
Cornwell, J. C.	Nye, S. D.†
Ehlers, H. H.	Owens, E. B.
Fahey, R. E.	Plonko, M. C.
Farrell, L. B.	Reed, T. B.
Finn, M. C.	Roddy, J. T.
Fischler, S.	Siuta, V. P.†

GROUP 84
SOLID STATE SPECTROSCOPY

J. G. Mavroides, *Leader*
G. B. Wright, *Assistant Leader*

Curran, E. A.	Halpern, J.‡
Dickey, D. H.	Kolesar, D. F.
Dimmock, J. O.	Krag, W. E.
Dresselhaus, M. S.	Mason, W. C.
Edwards, D. F.	Mastromattei, E. L.
Fulton, M. J.	Scouler, W. J.

GROUP 85
APPLIED PHYSICS

R. H. Rediker, *Leader*
R. J. Keyes, *Assistant Leader*

Bates, D. H.	May, W. G.†
Butler, J. F.	Melngailis, I.
Calawa, A. R.	Palermo, J. S.
Caswell, F. H.	Phelan, R. J., Jr.
Clough, T. F.	Quist, T. M.
Donaldson, P. L.	Sirrine, R. C.
Foyt, A. G.‡	Stopek, S.
Grant, C. R.	Sullivan, F. M.
Hinkley, E. D., Jr.	Ward, J. H. R., III
Hurwitz, C. E.	Youtz, P.

GROUP 86
OPTICS AND INFRARED

R. H. Kingston, *Leader*
F. L. McNamara, *Associate Leader*
M. M. Litvak, *Assistant Leader*

Billups, R. R.	Soref, R. A.
Chatterton, E. J., Jr.	Tank, C. C. M.
Dennis, J. H.	Underwood, D. I.
Longaker, P. R.	Wong, G. W.
O'Connor, J. R.	Ziegler, H. L.
Pitts, R. F.	Zieman, H. E.
Rotstein, J.	Zimmerman, M. D.
Schlickman, J. J.	

---

* Part Time
† Research Assistant
‡ Staff Associate

I. SOLID STATE DEVICE RESEARCH

A. SPECTRAL LINEWIDTH AND FREQUENCY STABILITY OF GaAs LASER

The spectral width of the CW GaAs laser line at 8374 Å has been found to be narrower than the resolution obtainable by grating spectrometer techniques. We have used a gas-driven Fabry-Perot interferometer to obtain a better indication of the true linewidth of the radiation from a GaAs diode laser at liquid-helium temperature. By observing the intensity of the center fringe with a 7102 photomultiplier, as a function of gas pressure, the spectrum in the vicinity of 8370 Å was obtained (Fig. I-1). The linewidth measured by this technique was less than 0.016 Å, the limit of resolution of this particular interferometer. At present we do not understand the origin of the small weak line which is displaced approximately 0.04 Å from the main peak.

With a constant current through the laser and the Fabry-Perot set for one-half maximum transmission, as shown in Fig. I-1, the stability of the laser output was observed. Figure I-2 shows a plot of the output for a period of approximately five minutes. The variations in the output shown in Fig. I-2 are due to fluctuations in the total experimental setup including, in addition to those of the laser, the fluctuations in the optical alignment, power supply, photomultiplier, and the remainder of the recording electronics. Taking all this into account, Fig. I-2 does indicate a stable laser output. In fact, if one were to compare this stability with that of the 6328-Å line of a commercial gas He-Ne laser, he would conclude that the GaAs laser output stability was excellent.

Independent measurements by Engeler and Garfinkel,[1] using standard interferometer techniques with a 6-cm cavity, have yielded a resolution limited halfwidth for the GaAs laser emission line of about 0.007 Å. The particular Fabry-Perot cavity used in our experiment had a plate spacing of 7 mm. By using a longer cavity (1 meter) one can hope to obtain resolutions approaching 0.0001 Å or 6 Mcps. If yet higher resolution is required, beat frequency measurements between the laser line and a doppler-shifted line seem to be most appropriate.

<div align="right">

F. Zernike, Jr.[†]
T. M. Quist
R. J. Keyes

</div>

B. InAs LASER CHARACTERISTICS

The spatial distribution and intensity of the coherent radiation from InAs injection lasers at 4.2°K has been measured. The diodes were made by diffusing zinc into a cleaved (110) crystal plane and by cleaving along two other (110) planes perpendicular to the first to form the reflecting planes of the laser cavity. In order to provide good thermal contact the diodes were mounted on a copper stud. In this way, threshold current densities of about 300 amp cm^{-2} at 4.2°K have been obtained, and continuous operation with currents of several amperes achieved. All of the measurements were made at 4.2°K, i.e., where the lasers can be operated with continuous currents.
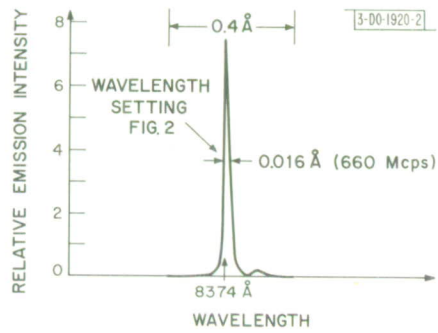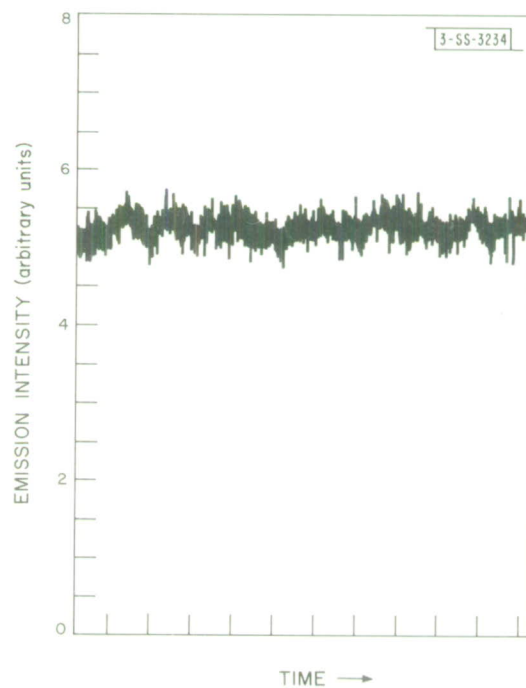

[†] Optical Maser Department, Perkin-Elmer Corp.

Fig. I-1. High resolution spectrum of CW GaAs laser operating at helium temperature.

Fig. I-2. Recorder trace indicating stability of CW GaAs laser at helium temperature. Fabry-Perot cavity set for one-half maximum transmission as shown in Fig. I-1.

The angular spread of the emission was measured by moving a photovoltaic InSb detector across the beam. Figure I-3 is the beam pattern in the plane of the junction for a diode at a current about 50 percent higher than the threshold. A measurement of the spectrum at this current indicated that most of the radiation was in a single-cavity mode. The angle at the half-power point of the beam pattern in Fig. I-3 is about 7°. The width of a slit which would produce a diffraction pattern of such an angle for 3.1-micron radiation is 26 microns. This means that only about one-fifth of the 125-micron wide junction is emitting at this current. By comparison (for GaAs laser diodes), one of the smallest angles in the junction plane which has been reported[2] is about three-fourths of a degree, corresponding to an emitting region of 40 microns for the 0.84-micron radiation. The fraction of the diode width emitting uniformly is probably related to the uniformity of the structure.

As the current is increased the spectrum, in most cases, shows multi-moding, and the diffraction pattern in the junction plane consists of multiple beams. Figure I-4 is a pattern for a diode operated at six times the threshold current. Such a pattern can result from multiple filaments in the junction. As Fenner and Kingsley have shown,[2] variations of phase and amplitude of the radiation along the junction width can produce very complex beam patterns (which they also observed in GaAs lasers).

The angular spread in the plane perpendicular to the junction, shown in Fig. I-5, is considerably larger than in the junction plane. If we disregard the superimposed structure, whose origin is uncertain, the beam is about 30° wide. This corresponds to an emitting region of 6 microns perpendicular to the junction. The emitting region is determined by the total penetration depth of the wave perpendicular to its direction of propagation inside the diode. The active region, where the population is inverted, is contained in the emitting region, and hence must be less than 6 microns. For GaAs lasers an angle of about 10°, corresponding to a 5-micron region, has been reported.
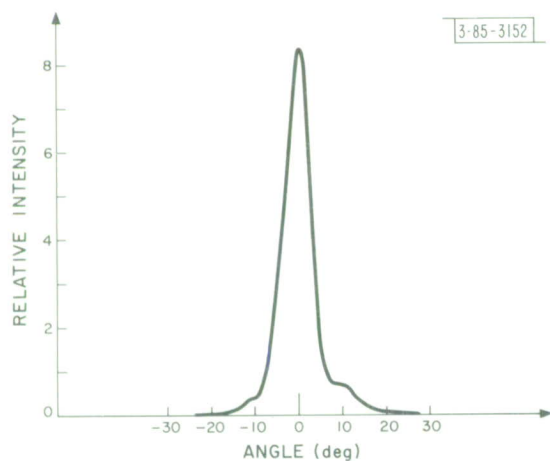
Fig. I-3. Radiation pattern in junction plane of InAs laser at 4.2°K with diode current 30 percent above threshold. Zero of angle scale has been arbitrarily set.
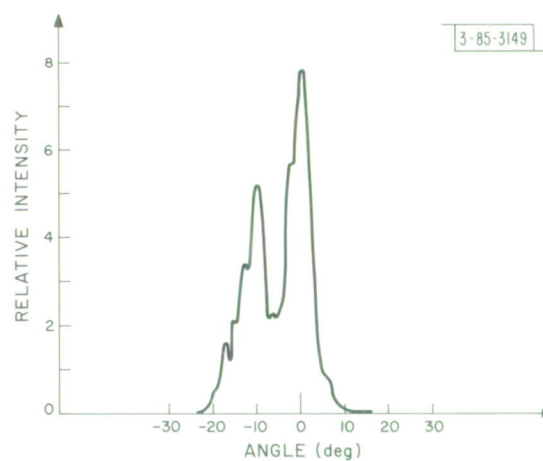
Fig. I-4. Radiation pattern in junction plane of InAs laser at six times the threshold current. Laser was operated at 4.2°K.
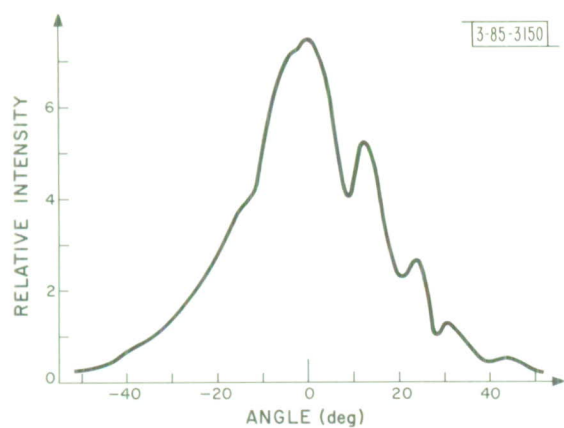
Fig. I-5. Radiation pattern in a plane perpendicular to junction plane of InAs laser operated at 4.2°K.

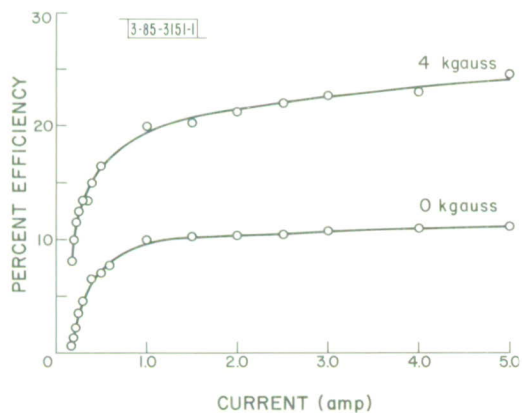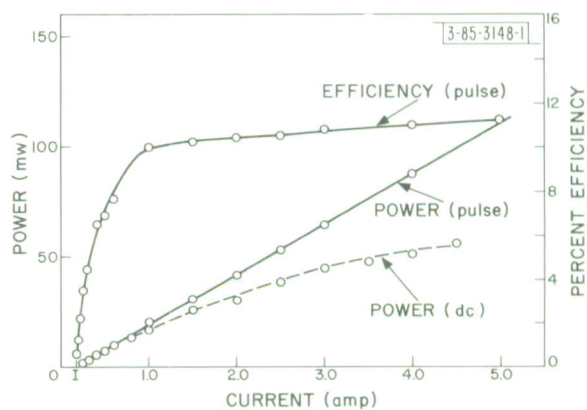Fig. I-6. Output power and external quantum efficiency of InAs laser at 4.2°K.

Fig. I-7. Effect of magnetic field on external efficiency of InAs laser at 4.2°K.

The absolute power emitted in the beam from one end of the diode was measured using a calibrated thermopile. Figure I-6 is a plot of total power in the beam and external quantum efficiency as a function of current. The efficiency, defined as the number of photons emitted per carrier crossing the junction, was computed assuming that all the radiation is concentrated in two beams of equal intensity, one emitted from each end of the diode. To prevent heating, the solid curves were obtained with pulsed currents. The power output obtained with DC is indicated by the dotted curve which shows the onset of heating, at about 1 amp. For currents above threshold, the efficiency first increases rapidly and then levels off. The highest efficiency is about 11 percent, compared with the highest value of 60 percent reported for GaAs lasers.[3]

We have previously noted that a magnetic field of a few kgauss applied perpendicular to the current flow in the diode reduces the threshold.[4] We believe this to be associated with the decrease of carrier diffusion due to Lorenz forces. Since the magnetic field produces an increase of intensity of the spontaneous radiation below threshold, but does not reduce the spontaneous linewidth, the concentration of carriers apparently increases the conversion efficiency at the junction. In diodes with lower threshold current densities, the percentage decrease of threshold caused by the magnetic field is less than in diodes with higher thresholds.

The magnetic effect also enhances the power output above threshold. The efficiency at 4 kgauss (Fig. I-7) is about a factor of two higher than at zero field but has nearly the same current dependence. From this value of efficiency in the saturation region, an _effective_ absorption coefficient in the diode bulk adjacent to the active region can be calculated.[5] Assuming a 100 percent conversion efficiency at the junction, the coefficient is about $50\,\text{cm}^{-1}$. Free carrier absorption in the n-type crystal has been measured[6] and found to be less than $10\,\text{cm}^{-1}$. Hence, it cannot account for this number ($50\,\text{cm}^{-1}$). A greater absorption is expected on the p-type side, but this is difficult to estimate because the impurity density varies with distance and is not accurately known. Because of a longer wavelength in InAs, a higher free carrier absorption is expected in comparison to GaAs. This may account for the somewhat lower efficiency of InAs lasers.

I. Melngailis

C. RADIATION FROM InAs DIODES INVOLVING OPTICAL PHONON EMISSION

In the previous Solid State Research report,[7] we reported that in the emission spectrum obtained from InAs diodes at 2°K an additional peak occurs at 0.372 ev, 28 mev below the main emission peak, and that a knee is observed at 0.34 ev. The 30-mev energy difference between the first satellite and the main peak agrees, within experimental error, with the energy of 29.5 ± 0.5 mev measured for a longitudinal optical phonon in InAs tunnel diodes by Hall, _et al._[8] A value of 28.8 mev has been determined for the phonon from optical-reflectivity data by Picus, _et al._[9] The second weaker satellite (60 mev below the main peak) corresponds to the energy of two longitudinal optical phonons, also observed in tunnel diodes,[8] at 59 ± 0.5 mev. The emission of these phonons can be expected in InAs, since it is a strongly polar compound and has a strong coupling of electrons to the lattice.
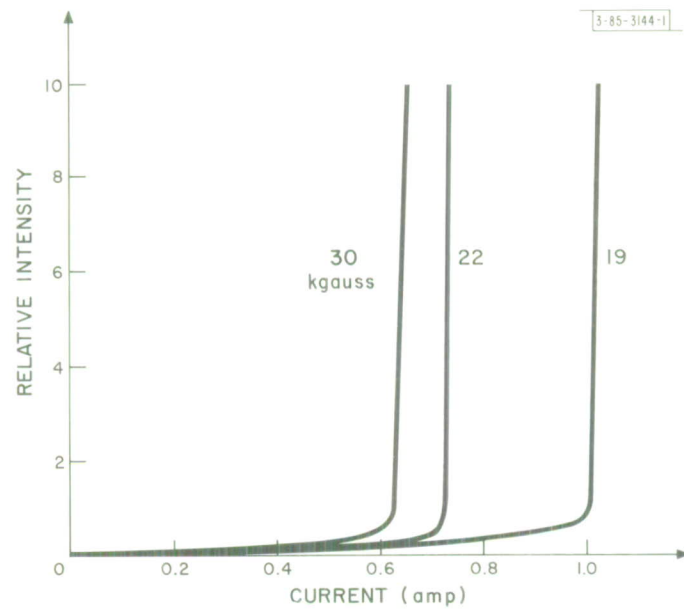
R. H. Rediker
I. Melngailis

Fig. I-8. CW emission from InSb diode laser at 2°K for three values of longitudinal magnetic field showing reduction of threshold current with increasing magnetic field.
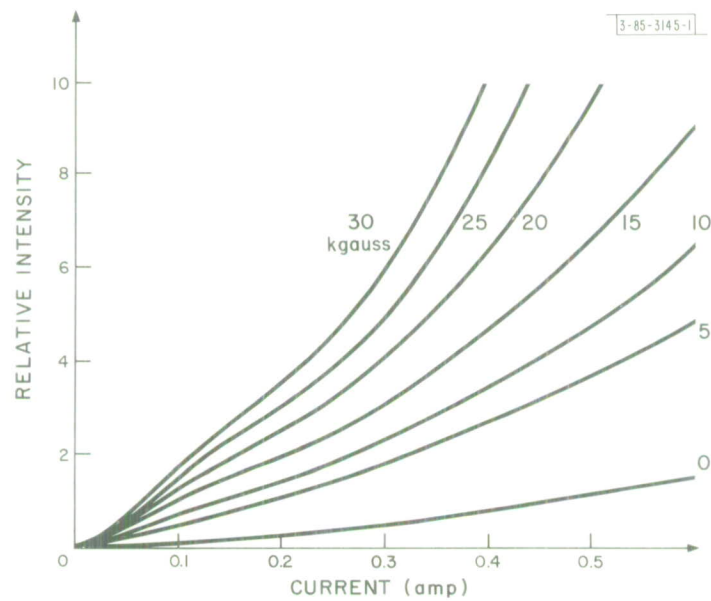

Fig. I-9 Emission intensity vs diode current below threshold for various values of longitudinal magnetic field.

D. MAGNETIC EFFECTS ON SPONTANEOUS EMISSION AND LASER THRESHOLD IN InSb DIODES

We have previously reported[10] the reduction of the threshold for laser action in InSb diodes using magnetic fields. Using a monochromator with greater resolution and a more sensitive detector system, the effect of the magnetic field on the luminescence and on the threshold for laser action has been studied in more detail.

With InAs diodes, a threshold reduction was reported[11] using magnetic fields perpendicular to the injected current. This reduction was attributed to a decrease in the diffusion length and a consequent concentration of the inverted region. For InSb diodes, the transverse magnetic field enhanced the luminescence for fields up to about 2 kgauss but then caused a decrease for greater magnetic fields. This decrease has been assumed to be due to an increase in the diode temperature caused by the large transverse magnetoresistance. However, using a magnetic field parallel to the current the radiation continues to rise with the magnetic field to the point where continuous laser radiation is possible.

Figure I-8 shows an effect of the magnetic field on the threshold for laser action. The diode was in contact with a helium bath at less than 2°K. Threshold currents for this diode and these magnetic fields are clearly defined. We can see that as the magnetic field is increased the threshold current is decreased.

The effect of the magnetic field on the diode emission below threshold is illustrated for the same diode in Fig. I-9; additional data are presented to cover the range of magnetic fields from zero to 30 kgauss. For magnetic fields above 5 kgauss, the curves of Fig. I-9 can be divided into two regions. In the first region the detected radiation is the spontaneous emission, and the output increases approximately linearly with current. In the second region, in which the output increases super-linearly, there are multiple reflections of the spontaneous emission between the ends of the cavity. In this region, which has been called the super-radiant region, oscillations with spacing between maxima corresponding to that expected for adjacent cavity modes are superposed on the spontaneous spectrum. It should be noted that for zero magnetic field there is no linear region, but the intensity varies as the 1.7 power of the current for all currents plotted.

The intensity of the spontaneous emission at 200-ma forward current of the diode of Fig. I-9 is plotted in Fig. I-10 as a function of the longitudinal magnetic field. For magnetic fields between 10 and 30 kgauss (the maximum field for which data are presented), the emission intensity at 200 ma is linear with magnetic field. This linear dependence is predicted for allowed transitions between spherical bands in a direct gap semiconductor.[12] The present results, however, cannot exclude allowed transitions via excitons. The super-linear region below 10 kgauss has not been explained but can be due, in part, to the reduction in diode-leakage current produced by fields of this magnitude.

In addition to increasing the luminescence intensity, the magnetic field narrows the emission spectrum. Figure I-11 shows the linewidth as a function of magnetic field. The linewidth narrows from about 5 to 2 mev as the magnetic field is increased from zero to 30 kgauss.

Theories for the threshold condition have been published which indicate that the threshold should be inversely proportional to the intensity at the lasing wavelength.[13] Assuming a

3-83-3195
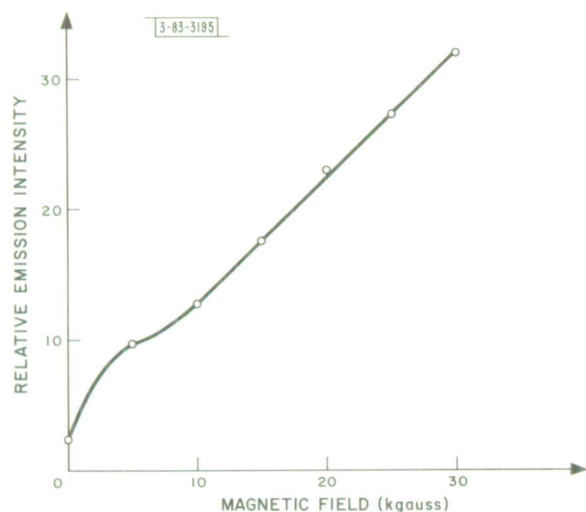
Fig. I-10. Emission intensity as a function of magnetic field for 200 ma current through InSb diode at 2°K.

Fig. I-11. Luminescence linewidth of radiation from InSb diode below threshold as a function of longitudinal magnetic field. Linewidth is plotted for 200 and 400 ma current through diode operated at 4.2°K.

3-85-3147-1
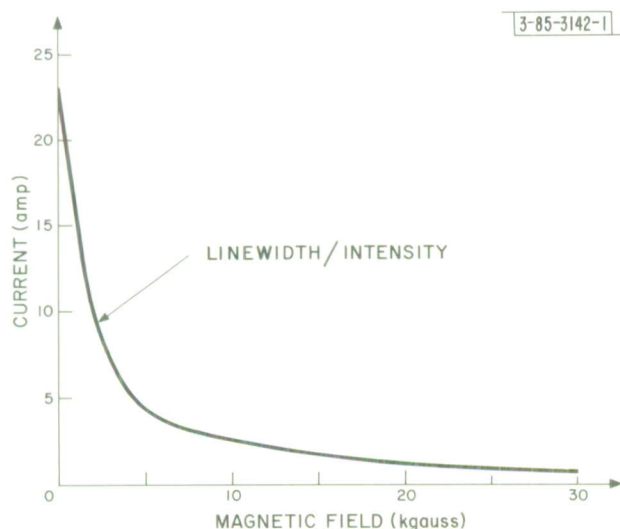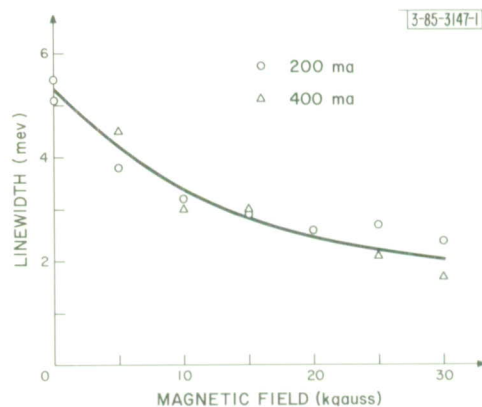
Fig. I-12. Threshold current as a function of magnetic field as predicted for measured intensities and linewidths (Figs. I-10 and I-11).

3-85-3142-1

8

Lorentzian shape for the luminescence spectrum, the threshold current should be inversely proportional to the total intensity and directly proportional to the linewidth. Figure I-12 shows how the threshold current is expected to vary as a function of magnetic field, from the measure intensities and linewidths of Figs. I-10 and I-11. We have matched the threshold with that at 30 kgauss. The advantage of using the magnetic field is clearly indicated. Where the diode took but 600 ma to lase at 30 kgauss, it would require over 20 amp to lase at zero magnetic field. Good quantitative data are not available to fit the curve for this range of magnetic fields since, although this diode operated continuously at 1 amp, pulses of 3-amp amplitude and 0.1-μsec duration caused heating and attenuation of the radiation. However, we previously reported data[10] for a more heavily doped diode in which heating effects are less. The change in the threshold with magnetic field showed, essentially, the behavior indicated in Fig. I-12.

In addition to increasing the efficiency and narrowing the linewidth, the magnetic field causes a splitting of the spontaneous line. Guillaume and Lavallard reported[14] that in some instances they observed, using pure samples, a splitting of the main line in a field of 8.6 kgauss. In addition, they noticed that the higher energy line increased its intensity with current. We reported[10] laser action from two such lines. By improving our system, we were able to study the luminescence in more detail and reproduced both lines from diodes made from cyrstals with n-type concentrations of both 10^{14} and 10^{16} per cm^3. The observation of the upper line requires a magnetic field strong enough to split the energy of the peaks greater than a value determined by the resolution of the monochromator and sufficient current to fill the lowest state and start to populate the higher state. There is, again, the condition that the heat transfer must be such that one can inject to the higher current densities without overheating the diode.

Figure I-13 shows three spectra of the below-threshold emission of an InSb diode. The sharp dips in the emission lines are due to the absorption by water in the atmosphere. The upper two spectra correspond to a magnetic field of 20 kgauss. The current for curve (a) is 1 amp. By increasing the current to 3 amp [curve (b)] the higher energy state is populated and the two emission lines are observed. Increasing the magnetic field to 25 kgauss [curve (c)] shifts both lines to higher energy and increases the relative amplitude of the lower energy line. This increase in the amplitude is expected because the density of states in the lowest magnetic sub-band is increased. Comparison of curves (a) and (b) shows that the energy of the peak of the lower energy line does not shift with increasing diode current. This result is corroborated by other data which indicate that the individual lines do not shift in energy with increasing current, although the average energy of the emission does increase. The separation between the two emission lines is 4.9 mev at 20 kgauss and 5.8 mev at 25 kgauss. This separation can be explained on the basis of spin splitting with an effective g value of about 40. This g value is lower than the value of 48 determined[15] for the lowest Landau level by extrapolation to zero magnetic field. To the accuracy of our measurements, since the g value is a decreasing function of magnetic field, the value of 40 is consistent with the radiative transitions associated with the spin-split lowest Landau level. These results should be compared with those of Guillaume and Lavallard[14] who, in order to explain their 5.2 mev splitting at 8.6 kgauss, postulated that the lower energy line was due to a transition from the donor band m = + 1/2 level, and the higher energy line was due to a transition from the first Landau m = −1/2 level.

9
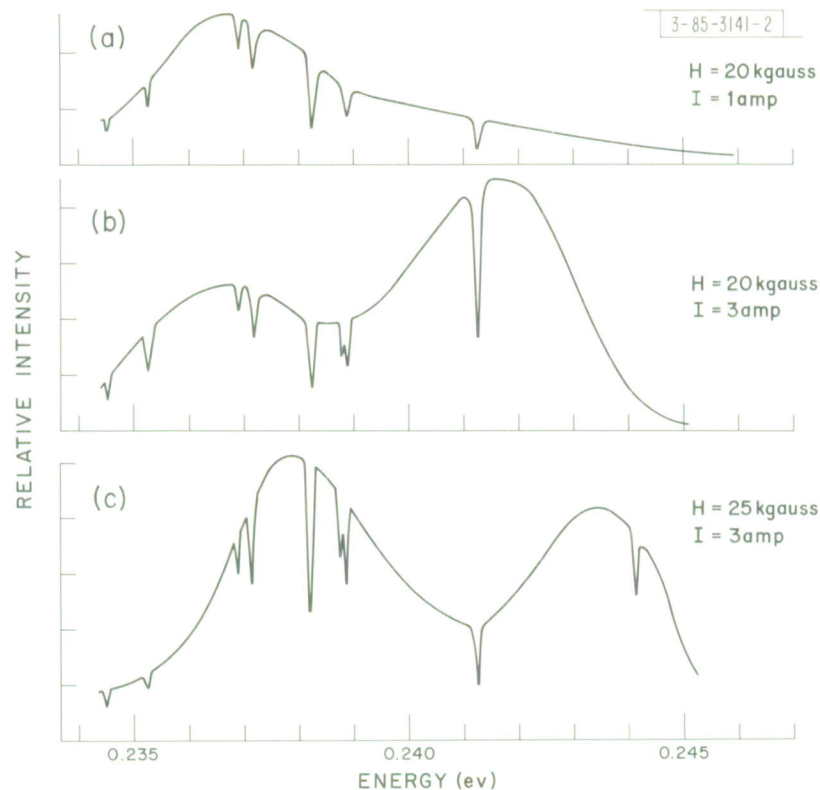
Fig. I-13. Spectra of luminescence emission from InSb diode below threshold. Sharp dips due to absorption by water in atmosphere. Diode was operated at 2°K.

The fact that the higher energy line (b) in Fig. I-13 is more intense than the lower energy line indicates that the transition probability from the higher energy spin state must be larger than that from the lower energy state. This can be interpreted[16] in terms of the spin selection rules and the spin of the terminal state associated with the valence band. The fact that laser action occurs first in the higher energy line[10] also indicated that the transition probability for radiative transitions from the higher energy state is larger than that from the lower energy state.

Published theories for the transition probability in a magnetic field for direct band-to-band allowed transitions (with and without excitons) include a predominant factor which increases linearly with magnetic field. The luminescent intensity is shown in Fig. I-10 to be a linear function of the magnetic field. The line narrowing of Fig. I-11 and the behavior of the spectra of Fig. I-13 are consistent with the expected condensation of states in a magnetic field. The diode luminescence data substantiate the view that the magnetic field increases the transition probability for radiative recombination and thereby lowers the threshold current for laser action.

R. J. Phelan
R. H. Rediker

E. INJECTION LUMINESCENCE IN PbSe AND PbTe

Low-intensity injection luminescence has been observed from forward-biased diffused diodes of PbSe and PbTe at 4.2°K. The diodes were fabricated by the method described in a previous report.[17] PbSe of both conductivity types was used as starting material and had 77°K carrier concentrations ranging from 5×10^{17} to $3 \times 10^{18} \, cm^{-3}$ and 77°K Hall mobilities between 33,000 and $12,000 \, cm^2 \, volt^{-1} \, sec^{-1}$. The single sample of PbTe used was p-type with a room-temperature hole concentration and Hall mobility of $3 \times 10^{18} \, cm^{-3}$ and $750 \, cm^2 \, volt^{-1} \, sec^{-1}$, respectively. The shallowest junction produced in PbSe was approximately 15 microns deep, and the junction depth of the single PbTe diode was about 100 microns.

The radiation was observed to emanate from the junction edges and could not be detected at the broad area faces of any of the diodes. This implies strong absorption by the bulk material. Because of the low intensity, the spectra have not yet been measured. However, the wavelengths of radiation have been estimated by measuring transmission through various filters. For PbSe injection luminescence, 2 mm of sapphire is opaque, 1.25 mm of LiF_2 allows 10 percent transmission, and 1 mm of CaF_2 allows 95 percent transmission. For PbTe luminescence, 2 mm of sapphire is opaque, and 1.25 mm of LiF_2 allows 95 percent transmission. From these results, the luminescence peaks can be placed between 6 and 7 microns for PbTe and 8 and 9 microns for PbSe.

<div align="right">J. Butler</div>

F. DESIGN OF LASER DIODES FOR HIGH-POWER EFFICIENCY

The principal mechanisms limiting the power efficiency of laser diodes are the series I^2R loss and the internal loss of photons by processes, such as free carrier absorption, that do not lead to subsequent re-emission. Restricting the discussion to these two types of losses, we consider the problem of choosing values for the diode dimensions, the current density, and the p- and n-type doping in order to produce a prescribed output power with as large an efficiency as possible. Let the junction be of length a in the amplifying direction and of width b in the transverse direction, and assume that the diode has unity internal quantum efficiency and is oscillating in nonlinear saturation. Then the power balance condition is

$$J(\hbar\omega/e) \, ab = (1 - R) \, P + \alpha * a\overline{P} \quad , \tag{1}$$

where J is the current density, P is the power incident on the surface, R is the surface reflectivity, $\overline{P}$ is the average power level in the interior, and $\alpha *$ is an effective absorption coefficient representing the loss due to processes such as free carrier absorption (as mentioned above). The external quantum efficiency is therefore

$$\eta_x = \frac{1 - R}{1 - R + \gamma\alpha * a} \quad , \tag{2}$$

where $\gamma = \overline{P}/P$. Hence, for high efficiency it is clear that both R and $\alpha * a$ must be small; otherwise, most of the power is lost internally. In the remainder of the discussion it will be assumed that dielectric coating, or some other method has been used to make $R \ll 1$, in which case it can be shown that $\gamma \approx 1/2$ and consequently

$$\eta_x \approx (1 + \tfrac{1}{2}\alpha * a)^{-1} \quad . \tag{3}$$

If I^2R losses are now included the total efficiency of the diode becomes

$$\eta_T = \frac{I(\hbar\omega/e)}{I(IR + \hbar\omega/e)}\ \eta_x \quad , \tag{4}$$

where it has been assumed that the voltage drop (quasi-Fermi level difference) at the junction is approximately $\hbar\omega/e$ (although, theoretically, it must be slightly in excess of this value). Writing $IR = J\rho d$, where d is the thickness of the diode and ρ is the average resistivity, and using (3), we have

$$\eta_T = [1 + (J\rho de/\hbar\omega)]^{-1}\ [1 + (\alpha*a/2)]^{-1} \quad . \tag{5}$$

If J is eliminated with the aid of (1), it is easily seen that η_T has a maximum as a function of a. The value of b should be as large as possible, but cannot exceed a if transverse oscillations are to be prevented. Setting b = a we find for the maximum value of η_T

$$(\eta_T)_{max} = [(1 + \beta/2)(1 + \beta)]^{-1} \quad , \tag{6}$$

where $\beta \equiv \alpha*a/2$ is the root of

$$\beta^3 - 2\beta c - 2c = 0 \quad , \tag{7}$$

with

$$c \equiv \frac{1}{4}\rho d\alpha*^2 P\left(\frac{e}{\hbar\omega}\right)^2 \quad . \tag{8}$$

When $c \ll 1$, $\beta \approx (2c)^{1/3}$ and $\eta_T \approx 1 - (3/2)(2c)^{1/3}$.

In order to proceed further we need to know how $\alpha*$ varies with concentration. If $\alpha*$ were due to free carriers only, then (8) indicates that the doping should be reduced until the corresponding values of a and b have been increased to the maximum that can be achieved technologically. However, if Turner and Reese's[18] interpretation of their optical absorption data is correct, then $\alpha*$ in n-type GaAs may be nearly constant at $5\,cm^{-1}$ for doping of $10^{18}\,cm^{-3}$ or less. In that case, the optimum n-type doping would be about $10^{18}\,cm^{-3}$. Turner and Reese also found that the free carrier absorption in p-type GaAs was about $3\,cm^{-1}$ for $1.6 \times 10^{18}\,cm^{-3}$ doping and about $40\,cm^{-1}$ for $1.6 \times 10^{19}\,cm^{-3}$ doping.

For purposes of illustration let us take as a design value P = 1 kw and choose GaAs of $10^{18}\,cm^{-3}$ n-type doping and $3 \times 10^{18}\,cm^{-3}$ p-type doping. The value of d should be as small as possible; we will assume the low, but feasible, value of 25 microns for the thickness of the n-type substrate and 5 microns for the p-type diffused layer. Then $\alpha* \approx 5\,cm^{-1}$ and $\rho d \approx 1.5 \times 10^{-5}$ ohm, from which one calculates c = 0.04, β = 0.5, and η_T = 0.5. This in turn gives a = b = 0.2 cm and $J = 2.5 \times 10^4\,amp\,cm^{-2}$. Since these numbers are all reasonable, pulsed outputs of 1 kw with 50-percent efficiency should be achievable. It should also be possible to obtain 100-watt output with 75-percent efficiency.

<div align="right">A. L. McWhorter</div>

REFERENCES

1. W. E. Engeler and M. Garfinkel, J. Appl. Phys. (to be published).

2. G. E. Fenner and J. D. Kingsley, J. Appl. Phys. 34, 3204 (1963).

3. S. V. Galginaitis, J. Appl. Phys. 35, 295 (1964).

4. I. Melngailis and R. H. Rediker, Appl. Phys. Letters 2, 202 (1963).

5. A. L. McWhorter, see Sec. I-F of this report.

6. J. R. Dixon and J. M. Ellis, Phys. Rev. 123, 1560 (1961).

7. Solid State Research Report, Lincoln Laboratory, M. I. T. (1963:4), p. 9.

8. R. N. Hall, J. H. Racette, and H. Ehrenreich, Phys. Rev. Letters 4, 456 (1960).

9. G. Picus, E. Burstein, B. W. Henvis, and M. Hass, J. Phys. Chem. Solids 8, 282 (1959).

10. R. J. Phelan, A. R. Calawa, R. H. Rediker, R. J. Keyes, and B. Lax, Appl. Phys. Letters 3, 143 (1963).

11. I. Melngailis and R. H. Rediker, Appl. Phys. Letters 2, 202 (1963).

12. R. J. Elliott, T. P. McLean, and G. G. MacFarlane, Proc. Phys. Soc. (London) 72, 553 (1958).

13. A. L. McWhorter, Solid-State Electronics 6, 417 (1963).

14. C. Benoit á la Guillaume and P. Lavallard, Proceedings of the Conference on the Physics of Semiconductors, Exeter (1962), p. 875.

15. S. Zwerdling, W. H. Kleiner, and J. P. Theriault, J. Appl. Phys. 32, 2118 (1961).

16. B. Lax, private communication.

17. Ref. 7, p. 13.

18. W. J. Turner and W. E. Reese, J. Appl. Phys. 35, 350 (1964).

II. LASER RESEARCH

A. RAMAN LASER

1. Parametric Interaction Between Stimulated Stokes and Anti-Stokes Radiation

The onset of stimulated emission of Stokes radiation in a resonant cavity structure has been previously considered in terms of the rate of stimulated emission of Raman quanta.[1] To consider more general situations, coupled-driven, vibrational-field and Maxwell-field equations must be considered. Noise-source terms must also be included. The coupled set of equations is of the form

$$i(\omega \pm \omega_v + i\Gamma_v) U_i^{\pm}(\vec{k}, \alpha) = \sum_{j\ell} \iint d\vec{k}'\, d\omega'\, a_{ij\ell}^{\pm}(\vec{k}, \vec{k}', \omega, \omega')\, E_j(\vec{k}', \omega')\, E_\ell(\vec{k} - \vec{k}', \omega - \omega')$$

$$+ N_i^{U\pm}(\vec{k}, \omega) \quad , \tag{1a}$$

$$\left(\vec{k}^2 - \frac{\omega^2}{v^2(\omega)}\right) E_i(\omega, \vec{k}) = \sum_{j\ell} \iint d\vec{k}'\, d\omega'\, b_{ij\ell}(\vec{k}, \vec{k}', \omega, \omega')$$

$$\times E_j(\vec{k}', \omega')\, U_\ell(\vec{k} - \vec{k}', \omega - \omega') \quad . \tag{1b}$$

Here, $U_i = U_i^+ + U_i^-$ is the vibrational-field Fourier component and $N_i^{U\pm}$ is a noise-source Fourier component representing spontaneous vibrational excitation. The vibrational field U represents the excitation of either an internal vibration of a molecule in a system of organic molecules, or an optical phonon in a solid. In an ionic system, it may also represent a wave of excitation between two crystal field levels on the ions. The nonlinear driving term in (1a) represents a nonlinearity of the vibrational excitation, due to the presence of higher energy levels of the system, which appears in perturbation theory. The nonlinear driving term in (1b) represents a nonlinearity of the polarizability of the Raman-active medium proportional to the amplitude of excitation of the vibrations of the system.

Since the dispersion term in U is negligible for the usual flat spectrum of weakly coupled oscillators it has been neglected in (1a), and the vibrational field U can be eliminated in (1a) and (1b) to give

$$\left(\vec{k}^2 - \frac{\omega^2}{v^2(\omega)}\right) E_i(\vec{k}, \omega) = \sum_{jmn} \iiiint d\vec{k}'\, d\omega'\, d\vec{k}''\, d\omega''\, \chi_{ijmn}\, E_j(\vec{k}', \omega')\, E_m(\vec{k}'', \omega'')$$

$$\times E_n(\vec{k} - \vec{k}' - \vec{k}'', \omega - \omega' - \omega'') + N_i(\vec{k}, \omega) \quad , \tag{2}$$

15

where

$$\chi_{ijmn} = \sum_{j\ell+-} \frac{b_{ij\ell}(\vec{k}, \vec{k}', \omega, \omega')\, a^{\pm}_{\ell mn}(\vec{k} - \vec{k}', \vec{k}'', \omega - \omega', \omega'')}{i(\omega - \omega' \pm \omega_v + i\Gamma_v)} \quad ,$$

and

$$N_i(\vec{k}, \omega) = \sum_{j\ell+-} \frac{b_{ij\ell}(\vec{k}, \vec{k}', \omega, \omega')\, N^{U\pm}_{\ell}(\vec{k} - \vec{k}', \omega - \omega')\, E_j(\vec{k}', \omega')}{i(\omega - \omega' \pm \omega_v + i\Gamma_v)} \quad .$$

At this point it must be noted that the noise term in (2) cannot be considered in a classical way but must be considered quantum mechanically. The noise-source term will be larger in the Stokes case than in the anti-Stokes case in the ratio $\exp[-\hbar\omega_v/kT]$. When (2) is applied to the case of a Stokes − anti-Stokes system driven by a laser source of sharp frequency ω_L and wave vector $\vec{k}_L$, we obtain

$$\left[\vec{k}^2 + 2i k \overleftrightarrow{\gamma}(\omega) - \frac{\omega^2}{v^2(\omega)}\right] \vec{E}(\vec{k}, \omega) = \overleftrightarrow{K}(\omega)\, \vec{E}^*(\vec{k}', \omega') + \vec{N}(\vec{k}, \omega) \tag{3a}$$

$$\left[\vec{k'}^2 - 2i k' \overleftrightarrow{\gamma}(\omega) - \frac{\omega'^2}{v^2(\omega')}\right] \vec{E}^*(\vec{k}', \omega') = \overleftrightarrow{K}^*(\omega')\, \vec{E}(\vec{k}, \omega) + \vec{N}(\vec{k}', \omega') \quad , \tag{3b}$$

where

$$\vec{k} + \vec{k}' = 2\vec{k}_L \quad , \qquad \omega + \omega' = 2\omega_L \quad , \tag{4}$$

$$\gamma_{in}(\omega) = \frac{1}{k} \sum_{j,m} \chi_{ijmn}\, E_j(\vec{k}_L, \omega_L)\, E_m(-\vec{k}_L, -\omega_L) \quad , \tag{5}$$

and

$$K_{in}(\omega) = 2 \sum_{j,m} \chi_{ijmn}\, E_j(\vec{k}_L, \omega_L)\, E_m(\vec{k}_L, \omega_L) \quad . \tag{6}$$

In Eq. (3a) the $\overleftrightarrow{\gamma}(\omega)$ term acts as a parametric-growth term for the Stokes field $\vec{E}(\vec{k}, \omega)$, and in (3b) $\overleftrightarrow{\gamma}(\omega)$ gives a parametric damping term for the anti-Stokes field $\vec{E}(\vec{k}', \omega')$. This corresponds to the fact that the normal thermal population of levels of the Raman-active system favors emission over reabsorption for a Stokes process, and vice versa for the anti-Stokes process. The importance of phase matching is apparent in (3b), for a Stokes field which has been generated by the parametric gain in (3a) will excite a large anti-Stokes field in (3b) only if the phase matching condition $\vec{k'}^2 \sim [\omega'^2/v^2(\omega')]$ is satisfied.

Equations (3a) and (3b) also point up the difference between the Raman process for the generation of anti-Stokes radiation and a so-called four-photon process. In a four-photon

process, only virtual intermediate vibrational excitation is involved; the parametric terms involving $\overleftrightarrow{\gamma}$ will be absent in (3a) and (3b). This means that anti-Stokes and Stokes radiation can only appear in simultaneous, phase-matched rings. This is contrary to the observation of a distribution of Stokes quanta about the direction of the laser beam in stimulated Raman-scattering experiments.[2]

Equations (3a) and (3b) are being applied to a three-dimensional model of the traveling-wave growth of Stokes and anti-Stokes emission in a Raman-active medium driven by an intense laser source. In this model, the incoherently emitted Stokes photons induced by the laser beam act as sources of Stokes noise $N(\vec{k}, \omega)$ to be amplified by the growth term in (3a). The coupling of the anti-Stokes field to the Stokes field then causes a growth of the anti-Stokes wave.

As an initial approach to the analysis of this model, the growth of the Stokes wave according to (3a) is considered — neglecting the coupling to the anti-Stokes field which is based on a physical argument. The Stokes field then acts as a source term for the generation of anti-Stokes radiation, according to (3b). The physical argument for this decoupling is based on the fact that each noise source is considered incoherent with respect to the others. As a Stokes wave grows, it generates an anti-Stokes wave in a narrow cone-shaped region about the source with an angle corresponding to the Stokes phase matching direction. The anti-Stokes radiation quickly leaves this cone; therefore, the region of coherent interaction of the anti-Stokes wave back on the Stokes wave is small. We have examined this model for the following simple situation. We take the region in which the laser radiation is spherical (as in Fig. II-1) and calculate the growth of the Stokes wave and the resulting anti-Stokes wave. In Fig. II-1, $\vec{r}$ is the source point for the anti-Stokes wave and $\vec{s}$ is the observation point. In what follows we will, for simplicity, treat the field as a scalar quantity.

3-SS-3235

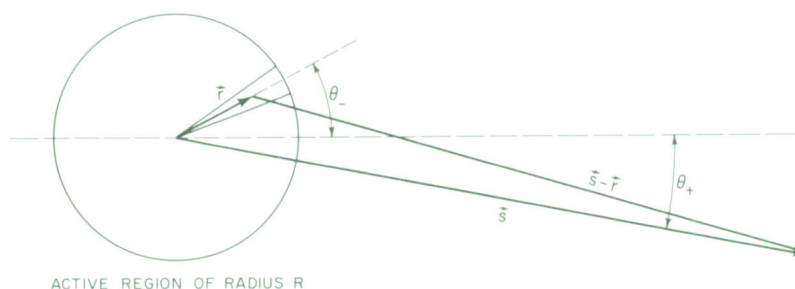ACTIVE REGION OF RADIUS R

Fig. II-1. Simple model for the growth of Stokes and anti-Stokes radiation.

The spatial part of the Stokes field E_- is given by

$$E_-(\vec{r}) = \frac{E_-^0}{4\pi} \frac{e^{ik_- r}}{k_- r} \quad , \tag{7}$$

where $k_- = i\alpha_- + \beta_-$, $\alpha_- = -\gamma(\omega_-)$, $\beta_- \cong \omega_-/v(\omega_-)$, and $\omega_- = \omega_L - \omega_v$. Note that we expect

$$|K_{\pm}| \cong 2\,|\beta_{\pm}\gamma_{\pm}| \quad . \tag{8}$$

Also, E_-^0 is the Fourier transform of the noise-source function $N(\vec{k}_-, \omega_-)$. Substituting (7) as a source term in the Fourier transform of (3b) we obtain, after integrating over the active region R and assuming $Rs^{-1} \ll 1$,

$$s^2\,|E_+(s)|^2 \cong \frac{|K(\omega_+)|\,|E_-^0|^2}{\beta_-^2(\beta_+^2 + 4k_L^2 - 4k_L\beta_+ \cos\Theta_+)}$$

$$\times \frac{1}{[(\beta_+^2 + 4k_L^2 - 4k_L\beta_+ \cos\Theta_+)^{1/2} - \beta_-]^2 + (\alpha_- - \alpha_+)^2} \quad , \tag{9}$$

where the $+$ sign indicates the anti-Stokes radiation. The above equation shows a sharp peak when

$$\cos\Theta_+ = \frac{\beta_+^2 - 4k_L^2 - \beta_-^2}{4k_L\beta_+} \tag{10}$$

and enables us to estimate the constant α_- and α_+ from experimental measurements of the angular width of the anti-Stokes peak (provided the spherical model does not oversimplify the present result for the width of the peak).

We will report further on the detailed calculation of (9) and a method of obtaining E_-^0 in terms of α_- using a generalization of the fluctuation dissipation theorem. We can thus connect the experimental anti-Stokes line width with the radiated Stokes power.

P. L. Kelley
H. A. Haus†
H. J. Zeiger

2. Off-Axis Stimulated Emission Experiments

It is of great theoretical and practical interest to obtain stimulated Raman emission in directions away from the direction of the incident laser beam. The experimental arrangement shown in Fig. II-2 has so far produced negative results. The generally smaller active pathlengths at
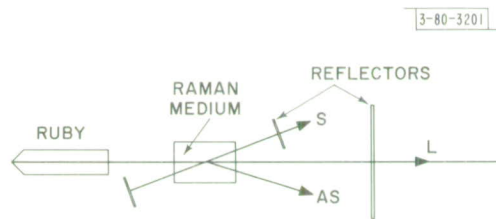

Fig. II-2. Experimental arrangement for obtaining off-axis stimulated Raman emission.

---

† Electrical Engineering Department, M.I.T.

some angle to the incident ruby beam will, of course, make the attainment of stimulated emission more difficult. But, an inability to overcome the threshold in a given situation may be attributable to the filamentary nature of the excitation in the Raman medium; the resulting transverse active pathlength in the Raman medium could thus be greatly diminished compared with the forward direction. In principle, there exists no reason why stimulated emission at an angle should not be attainable by a variety of experimental expedients. Therefore, the problem is being explored further.

<div align="right">
F. H. Perry
P. E. Tannenwald
H. J. Zeiger
</div>

3. Multiple-Pumped Raman Laser

The proposal by W. Culver, of the Institute for Defense Analysis (IDA), that the stimulated Raman emission from a number of primary ruby lasers incident on a common Raman-active medium can be added in phase is being investigated experimentally. A convenient configuration is one in which the Raman radiation is added up perpendicular to the incident ruby beams. This configuration will require that stimulated emission gain be obtainable at the Raman frequency perpendicular to the incident ruby beams; consequently, a preliminary experiment is being carried out with a single ruby laser and a transverse optical cavity. In order to overcome problems caused by the shorter active pathlength at 90° (compared to the forward direction when the Raman medium is inside the ruby optical cavity), an external focusing arrangement is used. Since a long active region is desired at 90°, and since the plane-parallel mirrors of the optical cavity at right angles favor plane wave modes, use of a cylindrical lens and its attendant focal line provides an optimum configuration.

<div align="right">
Jane H. Dennis
P. E. Tannenwald
</div>

4. Stimulated Raman Emission in Organic Liquids

Stimulated Raman emission has been observed from a variety of organic liquids such as toluene, acetone, bromoform, and chloroform.

Acetone gives rise to a Stokes and anti-Stokes line $2923\,cm^{-1}$ separated from the incident ruby wavelength. A large vibrational splitting is of interest because the electromagnetic radiation associated with the vibrational excitation, if it is observable at all, will be more easily detected in the near infrared.

Bromoform yielded a remarkable spectrum, i.e., a total of 23 stimulated emission lines were observed. The spectrum, photographed on Kodak High Speed Infrared film with a 1.5-meter Bausch and Lomb spectrograph, is shown in Fig. II-3. Eight Stokes and four anti-Stokes lines of one family are due to a vibrational excitation at $222\,cm^{-1}$; two Stokes and one anti-Stokes line belonging to a second family are due to a vibrational level at $541\,cm^{-1}$. Eight additional lines that can be identified on the original film are combination second-generation Raman lines produced by one family of lines scattered by the vibrational excitation of the other family. The origin of all combination Raman lines cannot be uniquely determined because a particular line can arise from either a $541\,cm^{-1}$ shift followed by a $222\,cm^{-1}$ shift, or by the reverse vibrational

3-82-3197

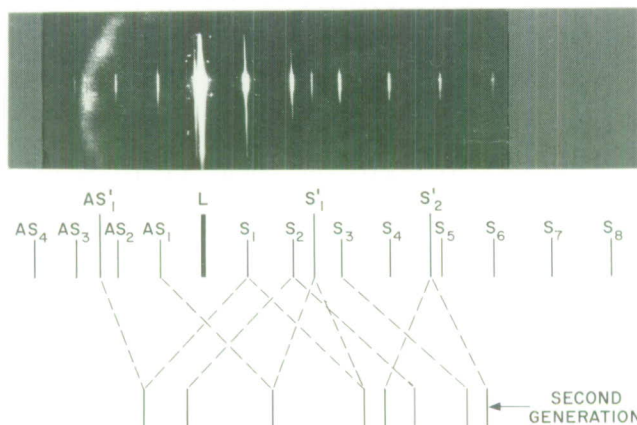STIMULATED RAMAN EMISSION IN BROMOFORM

Fig. II-3. Stimulated Raman emission spectrum in bromoform. Altogether, 23 Stokes and anti-Stokes could be identified in two separate films. The origin of all combination second-generation lines cannot be uniquely determined; e.g., a 222 cm^{-1} Stokes shift from AS_1' produces the same line as a 541 cm^{-1} anti-Stokes shift from S_1.

scattering order. This observation of the sum and difference of two vibrational frequencies of one molecule may be contrasted with the experiment of Stoicheff, who observed a similar effect upon mixing two separate liquids, benzene and carbon disulfide.[3]

S. Kern
B. Feldman

B. EVIDENCE OF SPECTRAL NARROWING FROM RUBY-EXCITED GaAs

The possibility of observing stimulated emission from optically excited GaAs has been discussed.[4] Experimental verification of such an effect by demonstrating line narrowing is complicated by the subthreshold narrowing action of the absorption edge on the internally generated radiation. As a result, this report will first discuss the magnitude of the subthreshold narrowing and then elaborate on several experiments involving the identification of true line narrowing originating in the band-edge emission of ruby-laser-excited GaAs.

Initially, a model 12-C Perkin-Elmer prism monochromator fitted with an RCA 7102 photomultiplier was used to obtain and compare the surface and cleaved-end emission from several p-type samples of GaAs. In particular, the end emission of the sample to be discussed was characterized by both a 60-Å spectral shift to a longer wavelength than the surface emission peak and a 20-percent decrease in linewidth (as compared to the surface emission linewidth). This phenomenon may be explained by considering the effect of the band-edge absorption coefficient[5] $\alpha(\nu)$ on the original lineshape. Qualitatively, since $\alpha(\nu)$ decreases rapidly with decreasing ν, the short wavelength side of the line is absorbed at a greater rate than the long wavelength side thereby modifying the fluorescent line. Moreover, a first-order approximation using a

Lorentzian line and path length $r_o \gg [0.1/\alpha(\nu_o)]$ has shown that the new maximum ν_m may be written as

$$\nu_m \sim \nu_o - \frac{\alpha(\nu_o)}{\frac{d\alpha}{d\nu}\left[1 - \alpha(\nu_o)r_o\left(\frac{\exp[-\alpha(\nu_o)r_o]}{1 - \exp[-\alpha(\nu_o)r_o]}\right)\right]} - \frac{\Delta\nu_o}{4} \quad ,$$

where ν_o is the surface emission peak, r_o the distance the radiation has traveled in the sample, and $\Delta\nu_o$ the surface emission linewidth. Therefore, when $\alpha(\nu)$ decreases due to the initiation of stimulated emission, the expected experimental data as a function of increasing power should be typified by a spectral shift back to near the surface emission peak plus the usual narrowing process.

The first experiment to demonstrate the above conclusion was obtained by immersing the cleaved sample in a liquid nitrogen bath and then optically pumping the polished surface with a normal mode, pulsed ruby laser.[6] The detector used was a Jarrell-Ash f/6.3 plane grating spectrograph equipped with 1-N spectroscopic plates. Table II-1 summarizes this experiment and indicates a factor of 2 decrease in the resultant linewidth and a spectral shift in the direction of the surface-emission peak. However, when the input power was increased the sample heated up, as evidenced by the shift to longer wavelengths and accompanying line broadening at a power density of 2×10^4 watts cm^{-2}. Furthermore, since multiple exposures were required to obtain the spectra, the background emission caused by the ruby spikes that were of too low an intensity to produce stimulated emission obscured the actual narrowing and made it difficult to take continuously varying data. As a result, the spectrograph was converted into a monochromator and a point-by-point study was made of the lineshape by simultaneously monitoring both the total fluorescent power at the entrance slit and the integrated partial powers at the exit slit. Table II-2 summarizes the point-by-point data and indicates the same behavior as the spectral plate data.

Experimental difficulties again precluded the gathering of continuously varying data, and a decision was made to try junction material in an attempt to enhance the magnitude of the previously observed effect. This decision was based on the possibility of an increase in the absorption depth under high intensity illumination,[7] the inherent ability of a semiconductor junction to guide light,[8] and the resulting simplified boundary conditions under reflection.[9] The experiment was performed on a laser diode chosen from a group of p-type indiffused junctions known to lase. It was prepared for optical excitation by removing the p-side assembly and then polishing the surface until spectroscopic studies and the expected diffusion behavior placed the junction depth at between 2 and 5 microns. Using a ruby laser as a source, two 1-N plates were taken of the cleaved end emission resulting in a background spectrum centered at 8433 Å and a linewidth of 124 Å. Superimposed on this spectrum were two distinct 8-Å slit-limited lines at 8406 and 8421 Å indicating possible oscillator behavior. Several tests were then conducted to clarify the origin of the lines, and in all cases the lines did not appear with the sample removed. However, subsequent testing using a Q-spoiled system permanently damaged the diode's surface.

In this manner, the experiments performed on ruby-excited GaAs have provided some evidence of line narrowing, although continuously varying data are required to substantiate the

TABLE II-1

FLUORESCENT EMISSION FROM CLEAVED p-TYPE GaAs EXCITED BY BOTH A TUNGSTEN LAMP AND RUBY LASER†

	Tungsten (Perkin-Elmer)		Ruby Laser (spectral plates)		
	Surface Emission	End Emission	Surface Emission	End Emission	
Power density (watts cm^{-2})	10^{-2}	10^{-2}	10^4	10^4	2×10^4
λ_o (Å)	8430	8490	8427	8463	8480
$\Delta\lambda$ (Å)	170	140	176	92	125

† The data are averaged over at least two measurements and the maximum error is ±5Å.

TABLE II-2

FLUORESCENT EMISSION FROM CLEAVED p-TYPE GaAs EXCITED BY A RUBY LASER†

	Ruby Laser (point-by-point)			
	Surface Emission	End Emission		
Power density (watts cm^{-2})	2×10^3	2×10^3	10^4	2×10^4
λ_o (Å)	8430	8460	8460	8490
$\Delta\lambda$ (Å)	200	150	75	100

† The data resolution is ±12Å.

results. At the same time, the experiments demonstrated the use of a normal mode, pulsed ruby laser as an expedient spectroscopic vehicle for order-of-magnitude measurements.

As a result of the observed data, new experiments are now in progress which place a greater emphasis on junction material and at the same time de-emphasize the use of a ruby pump. Simultaneously, full effort is being exerted toward the development of the noncoherent, quasi-continuous source described in Ref. 4 and designed for use in conjunction with the Perkin-Elmer monochromator.

J. J. Schlickman

C. THEORY OF MEASUREMENT OF ELECTROMAGNETIC FIELDS

The general, nonexclusive joint probability function $P(t_1, t_2, \ldots t_\ell) \Delta t_1 \Delta t_2 \ldots \Delta t_\ell$ for ℓ photoionizations was defined earlier[10] and used in an expression for the probability $P'_n(T)$ that n photo-ionization events occur in the time interval 0 to T. An explicit quantum-mechanical expression for a detector correlation function related to the correlation function[10] $\omega_1(t \mid x'x'')$ has since been derived.

The counting distribution $P'_n(T)$ was found[10] to be a compound Poisson distribution when the density operator for the field ρ is given in Glauber's P-representation,[11] that is, when ρ is represented as an incoherent mixture of coherent states. On the basis of this result, $P'_n(T)$ and some of its moments have since been evaluated further for possible use in analyzing experimental counting data. This has been done by making explicit assumptions about the form of Glauber's $P(\{\alpha\})$ function.[10] The following cases have been treated: (1) a coherent state; (2) an ideally incoherent field; (3) a spread-out coherent state; and (4) a state of the field with mode phases randomly distributed, mean mode amplitudes nonzero, and squared mode amplitudes having a Gaussian distribution. It is anticipated that the last-mentioned distribution may be particularly useful in describing counting data obtained in an He-Ne laser experiment[11] being conducted at the Laboratory.

W. H. Kleiner
P. L. Kelley

D. GASEOUS BREAKDOWN BY A GIANT-PULSED RUBY LASER

A study of the properties of the spark created during breakdown by a giant-pulsed ruby laser focused in air has been initiated. Shown in Fig. II-4 are oscilloscope traces of both the giant-pulse output and the spectral output as observed in the blue part of the visible spectrum. The rise time of the spark is approximately equal to that of the giant pulse, i.e., about 10 nsec. The decay of the spark is approximately exponential with a time constant of about 80 nsec — compared to the giant-pulse decay of about 10 nsec. This spark decay-time appears to be independent of laser peak power above breakdown threshold. The radiation emitted during this spark was measured qualitatively and found to be approximately "black body" on top of which was superimposed broad line spectra which extended out to wavelengths at least as long as 7 microns, the present limit of our instrumentation. Photographs of the spark taken with infrared-sensitive film and with film sensitive only in the visible indicate that the fire-ball, or spark, is nonuniform and has a definite reproducible structure. The peak power output of the giant-pulsed ruby was typically 20 to 30 Mw and the pulse width was 20 nsec. Sometimes the spark could be created with giant-pulse peak powers as small as 0.75 Mw.

D. F. Edwards

23

- SS - 3236

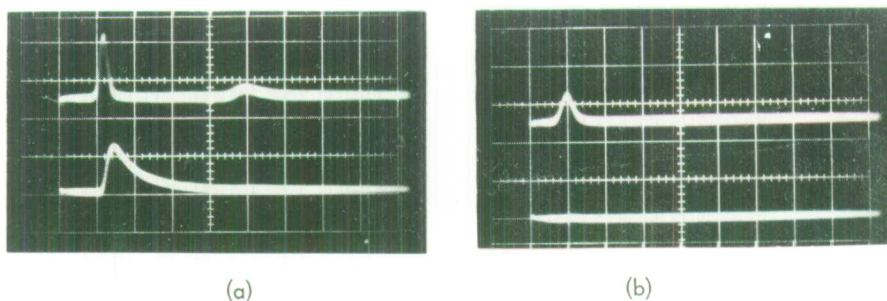(a)   (b)

Fig. II-4. Comparison of the light output from the giant-pulsed ruby with that of a spark in air as observed with a phototube with S1 phosphor and $CuSO_4$ filter. The upper trace in each photograph is the giant pulse and the lower trace is the spark. The time scale is 100 nsec cm^{-1}. In (a) the laser power output was above breakdown threshold while in (b) the laser power output was not sufficient for air breakdown.

| TABLE II-3 | | |
OPTICAL PROPERTIES OF Nd-DOPED LASER CRYSTALS		
Host Crystal	Wavelength of Emission (μ)	Polarization
$CaWO_4$	1.0586 1.0654	π σ
LaF_3	1.040 1.0634	σ π
SrF_2	1.0437	$\sigma\pi$
Glass	1.06 (broad)	$\sigma\pi$

E.   OPTICAL PROPERTIES OF Nd-DOPED LASERS

The giant-pulse and conventional laser properties of an Nd-doped glass rod 1/2-inch square × 12 inches long, were examined. This rod, furnished by Eastman Kodak, has typical fluorescence decay times (~65 μsec) as compared to ~450 μsec for one of American Optical laser glass. During conventional laser operation up to input energies as high as 40 percent above threshold, the Eastman Kodak rod output consisted of approximately uniformly spaced pulses. This same rod was operated under giant-pulse laser conditions by using a rotating prism. The pulse width (typically 40 to 50 nsec) was independent of the reflectivity, flashlamp input voltage, cavity length, and delay time between flashlamp firing and prism lineup. The largest peak power output measured was 17 Mw, but this does not represent the maximum available from this rod. At the time when the peak-power outputs were measured we were limited by the amount of energy that could be stored in the capacitor bank. The efficiency (light output energy/flashlamp input energy) of this particular Eastman Kodak glass, when operating as a giant-pulsed laser, was 0.014 percent. The energy stored in this rod was about 0.01 joules cm^{-3}. These figures may be compared with the following reported values for American Optical laser glass: efficiency ~0.3 percent and energy storage about 0.22 joules cm^{-3}.

The optical properties of several Nd-doped laser crystals were examined and compared with an Nd-doped $CaWO_4$ crystal. The wavelengths and polarizations are tabulated in Table II-3.

Here π and σ signify radiation which is plane-polarized-parallel and perpendicular, respectively, to the plane defined by the rod axis and the optical axis. Unpolarized light is referred to as $\sigma\pi$. The laser output from Nd-doped glass covers a spectral range that is wide compared to that of the crystalline host materials. The spectral width depends on the pumping energy.

<div align="right">D. F. Edwards</div>

F.   MAGNETIC-FIELD-INDUCED SECOND-HARMONIC GENERATION

A static magnetic field and the radiation from a Q-spoiled laser were applied to samples of GaAs and KDP in an effort to observe second-harmonic radiation whose intensity depended upon the static field. The crystallographic axes of the samples were oriented with respect to the electric vector of the linearly polarized laser light so that the portion of the harmonic intensity which depended solely upon the laser field would, in principle, vanish.

It was found that this portion of the intensity could only be reduced to about 1 percent of its maximum value, and the residual intensity was large enough to mask the static-field-dependent intensity when fields of up to 10 kgauss were used. This behavior is consistent with our calculations which show that the maximum static-field-dependent portion of the second-order dielectric polarization induced in the samples is smaller than the maximum field-independent portion by the factor ω_c/ω, where ω_c is the cyclotron resonance frequency of the electrons and ω is the optical frequency. The experiment will be repeated using phase-sensitive detection of the static-field-dependent intensity, provided that a CW or high-repetition-rate laser of sufficient output power becomes available.

<div align="right">R. Soref</div>

REFERENCES

1. Solid State Research Report, Lincoln Laboratory, M.I.T. (1962:2), p. 38, DDC 285456.

2. H.J. Zeiger, P.E. Tannenwald, S. Kern, and R. Herendeen, Phys. Rev. Letters $\underline{11}$, 419 (1963).

3. B.P. Stoicheff, Phys. Letters $\underline{7}$, 186 (1963).

4. Solid State Research Report, Lincoln Laboratory, M.I.T. (1963:2), DDC 417686.

5. W.J. Turner and W.E. Reese, J. Appl. Phys. $\underline{35}$, 350 (1964).

6. Solid State Research Report, Lincoln Laboratory, M.I.T. (1963:4), p. 25.

7. N.G. Basov and O.N. Krokhin, Soviet Phys. – Solid State $\underline{5}$, 1737 (1964).

8. A. Ashkin and M. Gershenzon, J. Appl. Phys. $\underline{34}$, 2116 (1963); A.L. McWhorter, Solid-State Electronics $\underline{6}$, 417 (1963).

9. H.M. Barlow and J. Brown, Radio Surface Waves (Oxford University Press, New York, 1962).

10. R.J. Glauber, Phys. Rev. $\underline{131}$, 2766 (1963).

11. C. Freed, private communication.

III. MATERIALS RESEARCH

A. INDUCTION PLASMA CRYSTAL GROWTH

1. Apparatus and Techniques

The original design[1] of the apparatus for growing refractory crystals with the induction plasma torch has been improved in several ways. The revised apparatus is shown schematically in Fig. III-1. The original powder feed tube, a quartz capillary which ended above the hottest part of the plasma (the "fireball"), has been replaced by a water-cooled stainless-steel hypodermic tube (0.030-inch i.d.) which extends to within about an inch of the growing crystal. Since the powder no longer passes through the fireball, its evaporation is greatly reduced. This increases the uniformity and efficiency with which powder is supplied to the crystal. Use of the tube also improves the stability of the plasma since, formerly, ionization of the powder affected the coupling of the plasma to the RF generator. The new arrangement also makes it possible to use the gas passing through the powder feed tube in order to change the composition of the ambient surrounding the crystal without changing the heat-transfer efficiency of the plasma, which is determined primarily by the composition of the fireball. This makes it easier to grow low-melting crystals which require oxidizing or reducing ambients because the heat-transfer efficiency is greatly increased by introducing gases other than argon into the fireball. Finally, the presence of the cold powder feed tube helps to center the plasma in the quartz nozzle which surrounds it. The outside diameter of this nozzle has been increased from about 1 to $1\frac{1}{2}$ inches. This makes it possible to increase the heat transfer without melting the nozzle, although a greater gas flow is required to achieve the same temperature. The RF-generator circuit has been modified by the incorporation of a variable capacitor. This was done since the plasma can be initiated and operated at much lower voltages by substituting a capacitance of 800 pf for the original value of 500 pf.

Difficulty is still being encountered in obtaining powders suitable for crystal growth. Such powders must be of high purity, have large enough particles to minimize evaporation in the plasma, and neither occlude nor release gases when they are melted and frozen. They must also flow well enough to be delivered at a satisfactory rate by the powder feeder. Many commercially available powders, particularly those prepared by wet chemical methods, do not meet these requirements. Some of these powders can be used if they are arc-melted in air or argon, depending on their chemical properties, and then reground. In order to use powders which cannot be delivered by the present powder feeder, but whose other properties are satisfactory, a new feeder is being constructed.

2. Divalent Transition Metal Oxides

Since the induction plasma torch can be operated over a wide range of gas compositions, we are investigating its application in growing crystals of the divalent oxides of the transition metals between titanium and nickel. The first few members of this series must be grown under neutral or reducing conditions to prevent oxidation to a higher valence, while the last members
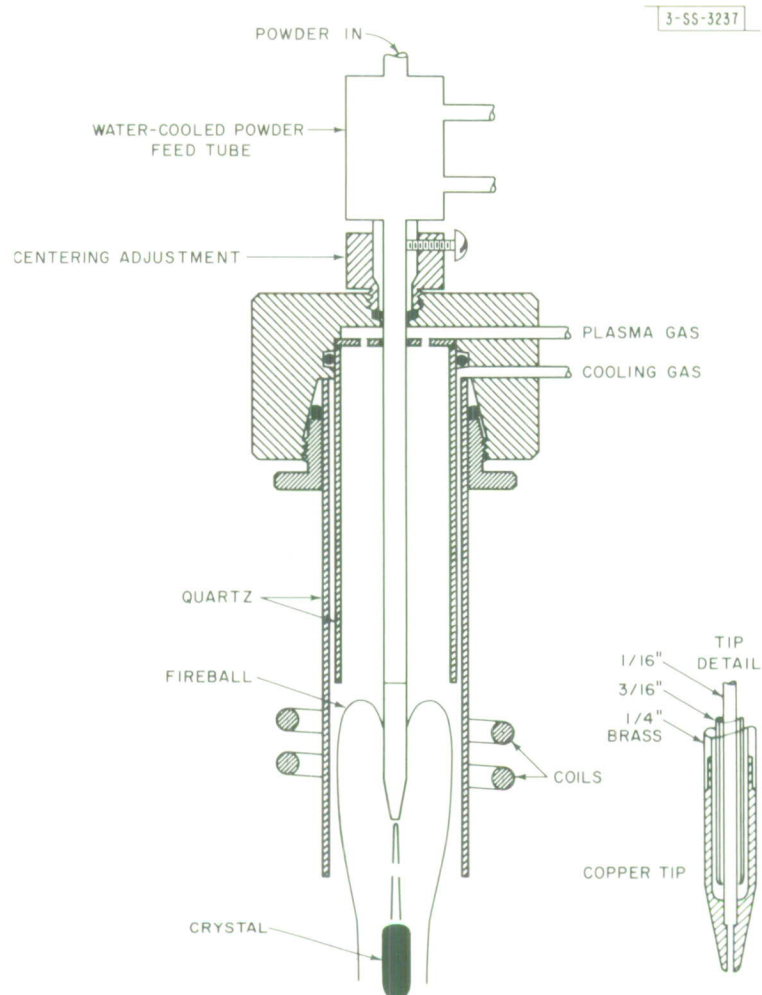
3-SS-3237

POWDER IN

WATER-COOLED POWDER FEED TUBE

CENTERING ADJUSTMENT

PLASMA GAS

COOLING GAS

QUARTZ

FIREBALL

COILS

CRYSTAL

TIP DETAIL

1/16"

3/16"

1/4" BRASS

COPPER TIP

Fig. III-1. Modified induction plasma torch used for growth of refractory crystals.
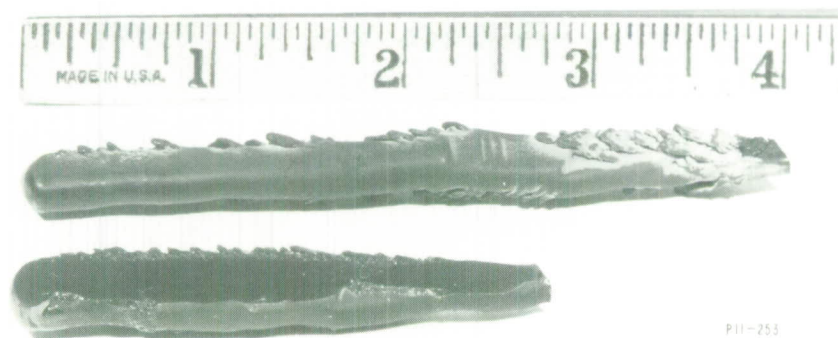
MADE IN U.S.A. 1 2 3 4

PII-253

Fig. III-2. Single crystals of MnO grown with induction plasma torch.

require strongly oxidizing ambients to prevent reduction to the metal. Considerable success has been achieved in initial experiments on MnO, CoO, and NiO.

Two single crystals of MnO, shown in Fig. III-2, were grown with an argon plasma using a powder feed gas consisting of 15 percent hydrogen and 85 percent argon. The powder was prepared by reducing very coarse MnO_2 powder in hydrogen for 16 hours at 1000°C. Both crystals grew along the $\langle 310 \rangle$ axis. They exhibit two external $\{100\}$ faces. They cleave on the $\{100\}$ plane, as can be seen in Fig. III-2. The as-grown crystals are black, but by transmitted light sufficiently thin sections are dark green and somewhat thicker sections are red.

Several crystals of CoO measuring about $1 \times 1 \times 4$ cm were grown with a 20 percent oxygen-80 percent argon plasma. They exhibit some porosity. No growth flats developed, but the cleavage is similar to that for MnO.

A number of NiO boules have been grown with a 20 percent oxygen-80 percent argon plasma using pure oxygen as the powder feed gas. Although large single-crystal regions were obtained, no boule is completely single. The material has the rocksalt (face-centered-cubic) structure. Crystals of NiO grown previously[2] with oxy-hydrogen flames were monoclinic. X-ray powder patterns do not reveal any metallic nickel in the majority of each boule. However, free nickel can be detected in the last-to-freeze portions, in spite of the strongly oxidizing atmosphere used. This suggests that the melt may have a significantly different composition from the solid.

<div align="right">T. B. Reed
R. E. Fahey</div>

B. OXIDE OF CHROMIUM WITH SPINEL STRUCTURE

Preparation of a form of CrO with rocksalt structure has been reported by Lux and Illmann.[3] This material, which was obtained by decomposition of $Cr(CO)_6$ at low temperatures, disproportionated to chromium and Cr_2O_3 above about 600°C. The other transition metals between titanium and nickel also have divalent oxides with rocksalt structure, but these compounds are all stable to high temperatures.

To determine whether CrO could be prepared by a high-temperature reaction between chromium and Cr_2O_3, equimolar quantities of these reagents were melted together under argon in an arc-melting furnace. A dense, black pellet was obtained. The x-ray powder pattern for this material contains no lines due to Cr_2O_3 and only one line due to chromium. All the remaining lines can be indexed on the basis of a spinel structure with $a_o = 8.379$ Å, as shown in Table III-1. No structure of this type has been reported for any oxide of chromium. Since Fe_3O_4 has a spinel structure with $a_o = 8.396$ Å, it seems likely that the new material is closer in composition to Cr_3O_4 than to CrO, although its stoichiometry has not yet been determined. A tetragonal form of Cr_3O_4 has been reported.[4]

When two powdered samples from the black pellet were heated in air for 64 hours at 1000°C, their weights increased by an average of 1.6 percent. Further heating for one week at 1100°C resulted in an additional weight gain of 0.8 percent. An x-ray powder pattern taken after this treatment contains some additional lines belonging to the spinel structure, shown in Table III-1. It also contains some lines due to chromium and Cr_2O_3. This observation suggests that some disproportionation occurred.

<div align="right">T. B. Reed
Mary C. Finn
R. E. Fahey</div>

		TABLE III-1			
		X-RAY DIFFRACTION DATA FOR OXIDE OF CHROMIUM (a_o = 8.379Å)			
		As Prepared		After Heating in Air[†]	
hkl	d_{calc} (Å)	d_{obs} (Å)	$100 (I/I_o)$	d_{obs} (Å)	$100 (I/I_o)$
111	4.84	4.75	40	4.85	50
220	2.962	2.96	10	2.956	10
311	2.526	2.50	100	2.520	100
222	2.419	2.40	10	2.417	5
400	2.095	2.10	40	2.097	80
331	1.922			1.922	5
333,511	1.612	1.61	40	1.609	30
440	1.481	1.48	40	1.481	50
533	1.278			1.273	20
444	1.209			1.213	10
711	1.173			1.180	20
731,553	1.091	1.092	40	1.091	20
800	1.047			1.048	10
555	0.966			0.964	5
840	0.938			0.938	5
911	0.919			0.919	5
931	0.878			0.878	5
844	0.856			0.856	5

[†]64 hours at 1000°C and 1 week at 1100°C.

C. THERMOELECTRIC PROPERTIES OF CrO_x

The preparation of CrO_2 by the reaction between equimolar quantities of CrO_3 and Cr_2O_3 under high pressure has been described previously.[5] By adjusting the ratio of CrO_3 to Cr_2O_3, the same procedure has been used to prepare hot-pressed polycrystalline samples of nominal composition $CrO_{1.87}$ and $CrO_{1.94}$. A platinum-foil liner was used in preparing the latter sample, in order to minimize contamination during the reaction. Both compositions have the same structure as CrO_2. The x-ray powder pattern for the $CrO_{1.94}$ sample did not reveal any second-phase material, but a trace of Cr_2O_3 could be detected in the $CrO_{1.87}$ sample.

The thermoelectric properties of both samples are very similar to those of CrO_2.[6] In Figs. III-3 and III-4 absolute values of the Seebeck coefficient are plotted against reciprocal absolute temperature for $CrO_{1.87}$ and $CrO_{1.94}$, respectively. In both cases the data can be represented by two straight lines which intersect at about 290°K. The resistivity of each sample

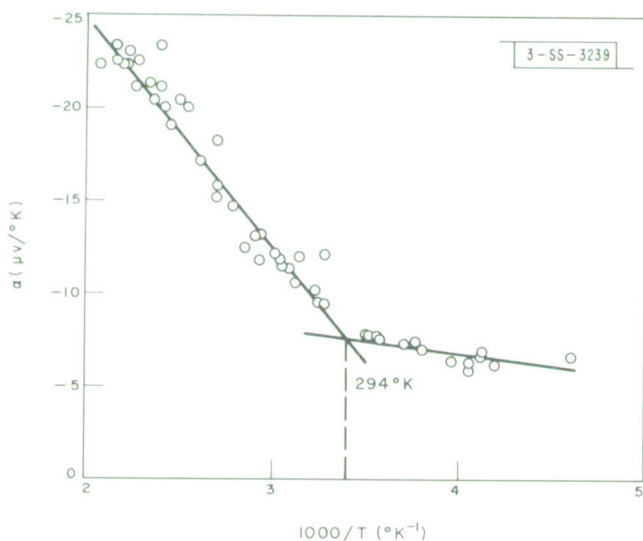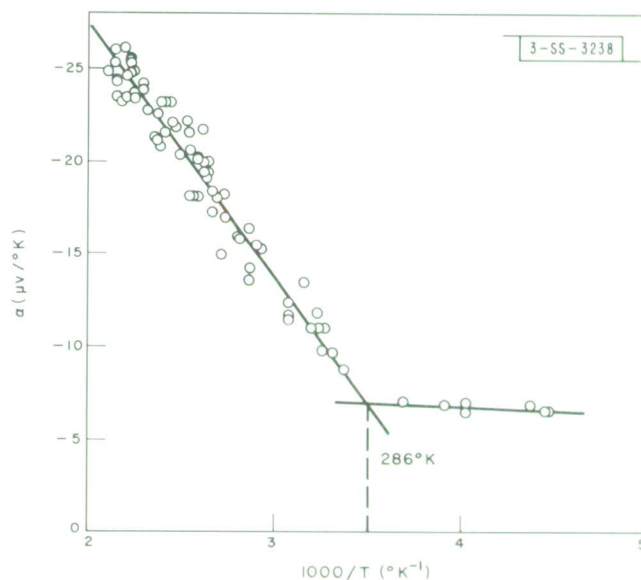Fig. III-3. Seebeck coefficient (α) vs reciprocal temperature for $CrO_{1.87}$ (nominal).

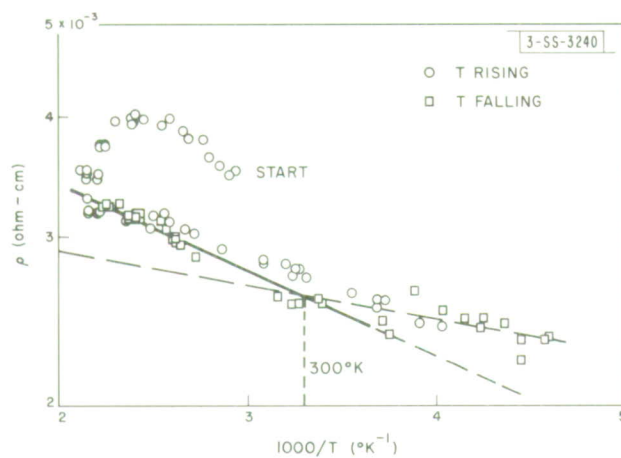Fig. III-4. Seebeck coefficient (α) vs reciprocal temperature for $CrO_{1.94}$ (nominal).

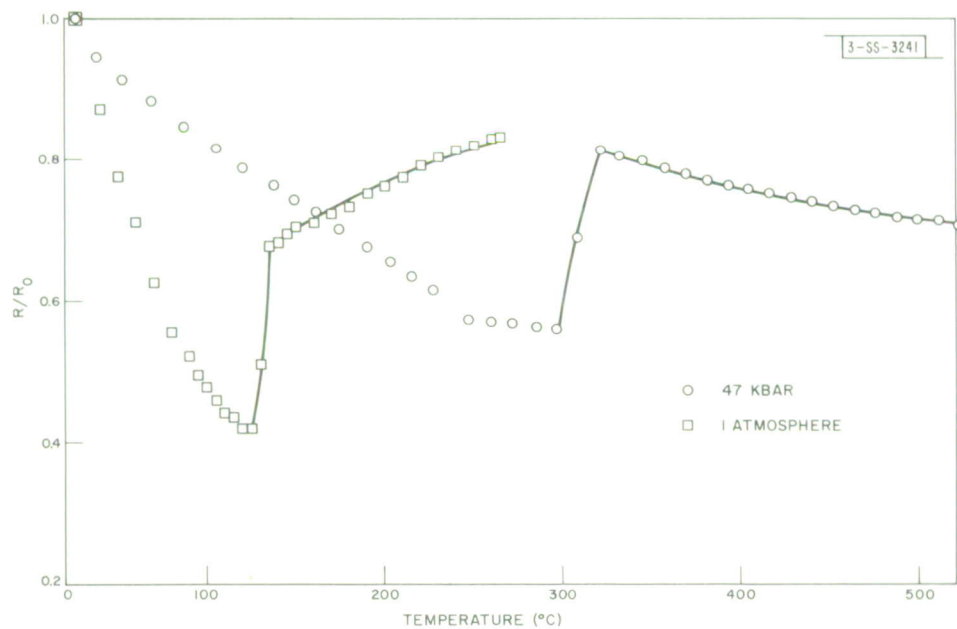Fig. III-5. Resistivity vs reciprocal temperature for $CrO_{1.87}$ (nominal).

Fig. III-6. Relative resistance (R/R_o) vs temperature for Ag_2Se at atmospheric pressure and at 47 kbar. At atmospheric pressure, resistivity in ohm-cm is equal to $(1.02 \times 10^{-3}) (R/R_o)$.

generally increases from about 2 to 9 milliohm-cm between $-60°$ and $+210°C$. Some hysteresis was observed for $CrO_{1.87}$ and still more for $CrO_{1.94}$. The logarithm of the resistivity of $CrO_{1.87}$ is plotted against reciprocal absolute temperature in Fig. III-5. The data can be fitted by two straight lines intersecting, in this case, at about $300°K$. The slopes of these lines correspond to activation energies of -6×10^{-3} and -2×10^{-2} ev in the low- and high-temperature regions, respectively.

<div style="text-align:right">

D. S. Chapin
J. A. Kafalas
J. M. Honig

</div>

D.   PRESSURE DEPENDENCE OF Ag_2Se TRANSITION TEMPERATURE

A sharp change in resistivity occurs when Ag_2Se is transformed from the low-temperature form (α-Ag_2Se) to the high-temperature form (β-Ag_2Se). Under atmospheric pressure, this transition occurs at about $130°C$. Resistance measurements have been used to determine the pressure dependence of the transition temperature for pressures up to 47 kbar. The samples were polycrystalline cylinders, cut from an ingot prepared by the horizontal Bridgman technique, with carrier concentrations of about 2×10^{18} cm^{-3} at $77°K$. Measurements of resistance vs temperature were made at atmospheric pressure by a 4-lead method, and those at higher pressures were made in the tetrahedral-anvil press by a 2-lead method previously used to investigate the pressure-temperature diagram of InSb.[7] (The 4-lead method was also used to measure room-temperature resistance as a function of pressure. No appreciable change in resistance was observed up to 40 kbar.)

Typical data for relative resistance vs temperature, obtained as the temperature was increased, are given in Fig. III-6 for atmospheric pressure and for 47 kbar. At all pressures the resistance increases sharply over a range of $15°$ to $20°C$ at the transition point, whereas Junod[8] and Baer and co-workers[9] observed a sharp decrease in resistivity in experiments at atmospheric pressure (although the resistivities which they measured just before the transition were approximately the same as in the present experiments). In agreement with the results of these workers, the temperature coefficient of resistivity at atmospheric pressure is negative for α-Ag_2Se and positive for β-Ag_2Se. This change in sign is also observed for pressures up to about 15 kbar, but at higher pressures the temperature coefficient is negative for both phases.

Transition temperatures obtained from the resistance-temperature curves for increasing temperature are plotted against pressure in Fig. III-7. For each pressure, the transition temperature was taken to be the temperature at which the resistance began to rise steeply. The increase in transition temperature with pressure is consistent with crystallographic evidence that β-Ag_2Se[10] is less dense than α-Ag_2Se.[11]

<div style="text-align:right">

M. D. Banus

</div>

E.   RATE OF CUBIC-TO-HEXAGONAL TRANSFORMATION IN $PrO_{1.5}$

When $PrO_{1.5}$ is prepared by reduction of Pr_6O_{11} either the stable hexagonal (A) form or the cubic (C) form may be produced, depending on the reaction temperature and other experimental conditions. The hexagonal form is generally obtained above $900°C$ and the cubic form below $600°C$, but in the intermediate temperature region the results of different workers are
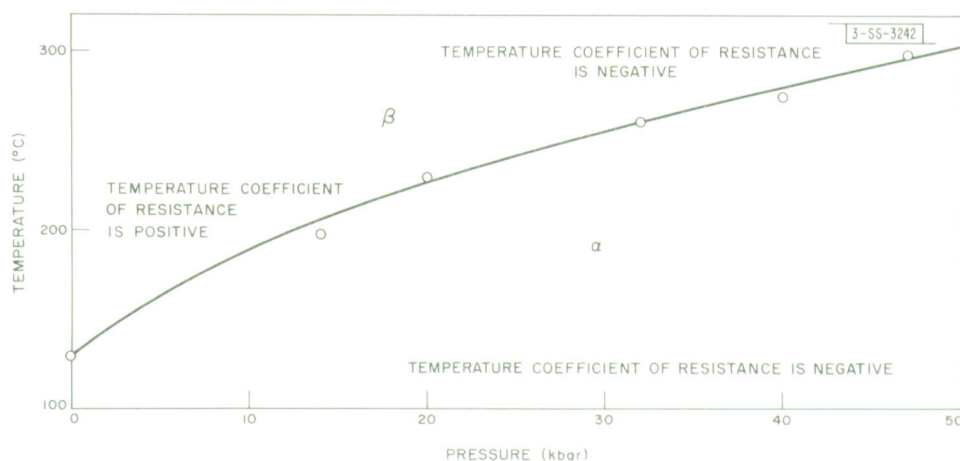
Fig. III-7. Temperature of α-β transition in Ag₂Se vs pressure.

Fig. III-7. Temperature of α-β transition in Ag_2Se vs pressure.

not consistent. In order to investigate the temperature dependence of the cubic-to-hexagonal transformation rate, freshly reduced samples of the cubic form were sealed under vacuum in quartz capillaries which had been outgassed at 1000°C. In order to exclude residual gases, particularly water vapor, the reduction was carried out for several days in a stream of hydrogen purified by diffusion through palladium. The apparatus was then evacuated, and the samples were transferred to the capillaries without being exposed to air. The samples were then annealed at elevated temperatures and quenched, after which their x-ray powder patterns were obtained without removing them from the capillaries.

According to the x-ray data, only a small fraction of the cubic phase had transformed to the hexagonal phase after heating for 96 hours at temperatures up to 775°C. Failure of other workers to prepare or retain the cubic phase at temperatures as high as 775°C is probably due to the presence of water vapor or oxygen at concentrations exceeding those of the current experiments. Most of the cubic phase had transformed after only 6 minutes at temperatures in the range 825° to 860°C. No evidence was obtained for a phase of $PrO_{1.5}$ with the same structure as the monoclinic (B) form observed for several other rare-earth sesquioxides.

D. S. Chapin
Mary C. Finn
J. M. Honig

F. SUPERCONDUCTIVITY OF In₄SbTe₃

F. SUPERCONDUCTIVITY OF In_4SbTe_3

The pseudo-binary InSb-InTe system contains a ternary compound with rocksalt structure which contains approximately 75 mol-percent InTe, corresponding to the nominal formula In_4SbTe_3.[12] This compound has been found to have an appreciable field of stability at high pressure, since lattice parameter measurements indicate that samples which were prepared at 37 kbar from melts of 75 and 80 mol-percent InTe contain In_4SbTe_3 as a single phase. Samples prepared at this pressure from melts of 60 and 85 mol-percent InTe are two-phase. In addition to In_4SbTe_3, these contain InSb and high-pressure cubic InTe(II),[13] respectively. (Single-phase samples with InTe(II) structure were obtained from melts containing 90 and 95 mol-percent InTe.)

According to data obtained by a self-inductance technique,[14] In_4SbTe_3 in the single-phase samples and in the two-phase sample containing InTe(II) exhibited superconductivity below about 1.5°K. The two-phase sample containing InSb failed to become superconducting down to 1.3°K (the lowest temperature investigated). These results indicate that the transition temperature of In_4SbTe_3 decreases with decreasing Te content.

The pseudo-binary InSb-InTe system has been investigated at atmospheric pressure by thermal, x-ray, and metallographic analysis. A tentative phase diagram is shown in Fig. III-8. In_4SbTe_3 is a peritectic compound unstable above about 550°C. Thermal arrests observed at 415° to 425°C indicate that it undergoes a solid-state transformation in that temperature region. The compounds InSb, In_4SbTe_3, and InTe are shown as line phases in the diagram, since their ranges of composition have not been established. (Thermal analysis and x-ray data indicate that InSb can dissolve up to 10 to 15 mol-percent InTe, but there is some evidence that the solid solutions are deficient in indium and actually lie in the $InSb-In_2Te_3$[15] pseudo-binary section.) Since cooling curves suggest that a second, unstable ternary compound may be formed from the melt between 50 and 70 mol-percent InTe, the liquidus in this region and a portion of the peritectic line are shown as dashed lines in Fig. III-8.

A single-phase sample of In_4SbTe_3 has been prepared at atmospheric pressure by directional crystallization of a melt initially containing approximately 40 mol-percent InTe. According to the tentative phase diagram, In_4SbTe_3 is not in equilibrium with melts of higher tellurium
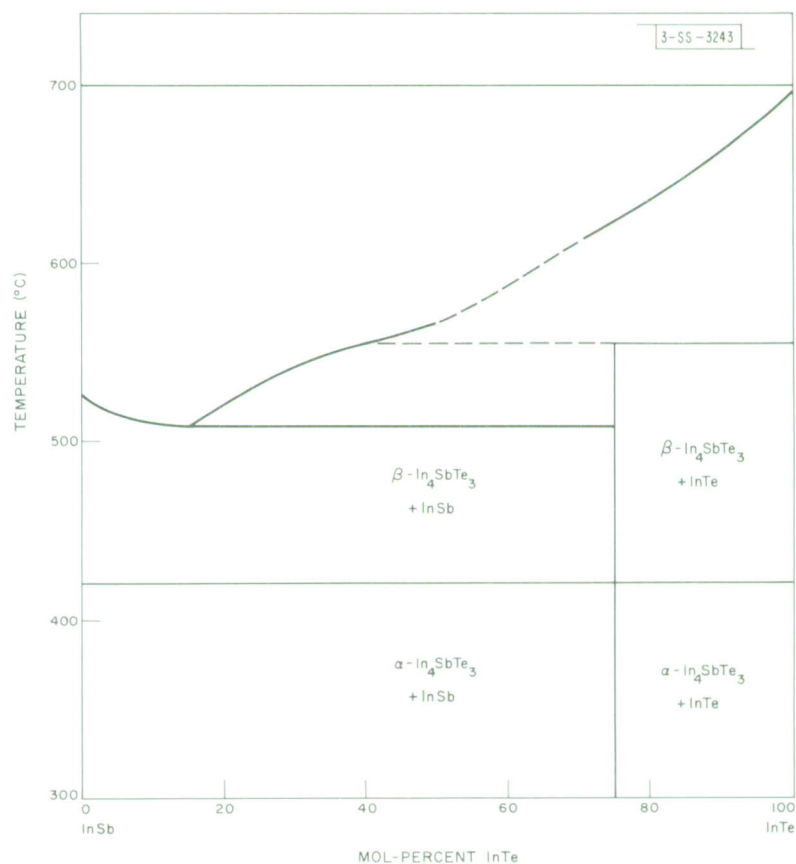

Fig. III-8. Tentative phase diagram of pseudo-binary InSb-InTe system.

content. The sample failed to become superconducting down to $1.3°K$ — a result which can be explained by assuming that the sample contains less tellurium than the high-pressure samples which exhibit superconductivity. This is a reasonable assumption, since the composition of the atmospheric-pressure sample must lie at the Sb-rich stability limit of In_4SbTe_3. It should be noted, however, that this sample has the same lattice constant, within the limits of experimental error, as the superconducting, high-pressure sample prepared from a melt of 75 mol-percent InTe.

M. D. Banus   Lynn B. Farrell
A. J. Strauss   M. C. Plonko
Mary C. Finn

G. PARTIAL PRESSURES IN THE Ge-Te SYSTEM

The partial pressures of $Te_2(g)$ and $GeTe(g)$ in equilibrium with condensed phases in the Ge-Te system have been determined by measuring the optical density of the vapor at wavelengths between 3100 and 4500 Å. The partial optical densities due to each species were evaluated and then converted to partial pressures by assuming Beer's law and published vapor pressure data for $Te(l)$[16] and $GeTe(c)$.[17] The same method has been used previously to measure partial pressures in the Pb-Te[18] and Sn-Te[19] systems.

The values of p_{Te_2} and p_{GeTe} measured for sample compositions of 1.00, 49.8, and 52.0 atomic percent tellurium are plotted against reciprocal absolute temperature in Figs. III-9 and III-10, respectively. Below $722°C$, the condensed phases are Te-saturated $GeTe(c)$ and Te-rich liquid for the 52.0 atomic percent tellurium sample and Ge-saturated $GeTe(c)$ and Te-saturated $Ge(c)$ for the other two compositions. Above $722°C$, the condensed phases for the 1.00 atomic percent tellurium sample are Te-saturated $Ge(c)$ and liquid, while the condensates for the other two samples are entirely liquid.

Over $GeTe(c)$ at its maximum melting point, $725°C$, p_{Te_2} is 0.6 ± 0.3 torr and p_{GeTe} is 17 torr. Below this temperature, p_{Te_2} over $GeTe(c)$ depends strongly on the composition of the solid phase. At $650°C$, for example, the value of p_{Te_2} over Te-saturated $GeTe(c)$ is about 20 times greater than the value over Ge-saturated $GeTe(c)$. The partial pressure of $GeTe(g)$, on the other hand, is the same, within experimental error, over both Te- and Ge-saturated $GeTe(c)$, and the data are represented by $\log p_{GeTe}$ (atm) $= -[(10.1 \pm 0.2)10^3]/T + 5.96$. If deviations from stoichiometry are neglected, this expression and the equation given below for $\Delta G°[GeTe(g)]$ lead to a standard Gibbs free energy of formation given by $\Delta G°[GeTe(c)] = (117.8 \pm 3) + 41.3 (10^{-3}) T$ kcal mole^{-1} for the reaction $Ge(g) + 1/2 Te_2(g) = GeTe(c)$. By comparing the slopes of $\log p_{GeTe} - 1/T$ plots above and below the melting point of $GeTe(c)$, the heat of fusion for the compound is found to be $11.3 + 2$ kcal mole^{-1}.

The measured values of p_{Te_2} and p_{GeTe} in equilibrium with Te-saturated $Ge(c)$ have been used to calculate the equilibrium constant and standard Gibbs free energy of dissociation for the reaction $GeTe(g) = Ge(g) + 1/2 Te_2(g)$. In these calculations p_{Ge} was taken to be equal to $p_{Ge}°$, the vapor pressure of pure $Ge(c)$. The difference between p_{Ge} and $p_{Ge}°$ should be much less than 1 percent, since Te-saturated $Ge(c)$ probably contains less than 0.1 atomic percent tellurium. Between $657°$ and $907°C$, $\Delta G°[GeTe(g)] = (71.5 \pm 2) - (14.0 \pm 1) 10^{-3}T$ kcal mole^{-1}. The standard enthalpy change of 71.5 ± 2 kcal mole^{-1} obtained from this equation has been combined with enthalpies calculated from spectroscopic data to obtain $D_o°[GeTe(g)]$, the energy
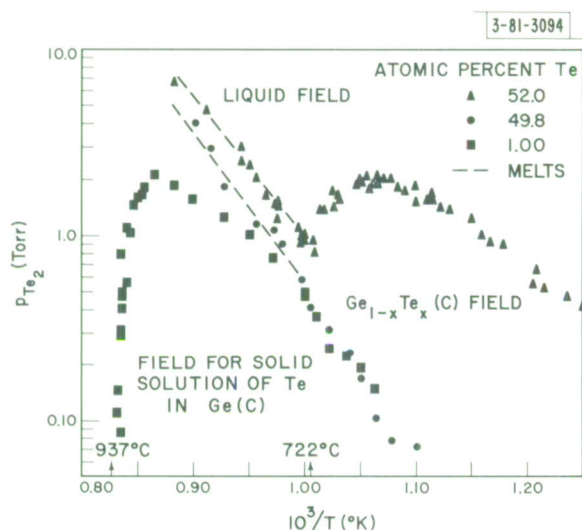
Fig. III-9. Partial pressures of $Te_2(g)$ for the Ge-Te system plotted against reciprocal absolute temperature.
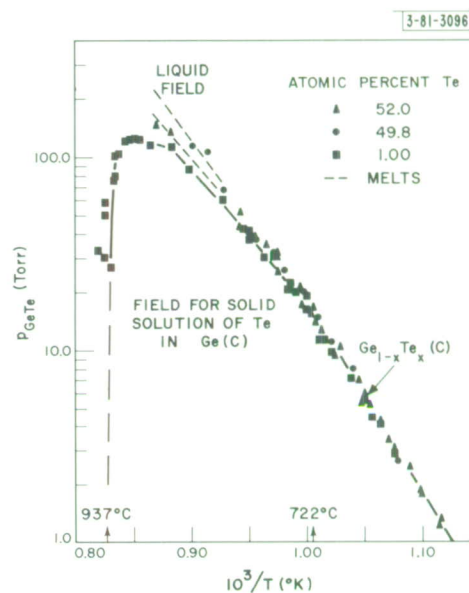
Fig. III-10. Partial pressures of GeTe(g) for the GeTe system plotted against reciprocal absolute temperature.

required to dissociate GeTe(g) into the gaseous monatomic elements at $0°K$. The value of D_o^o obtained in this manner is $95 \pm 4 \, kcal \, mole^{-1}$, in very good agreement with the value of $95 \pm 9 \, kcal \, mole^{-1}$ obtained by analyzing the electronic spectra of GeTe(g).[20]

R. F. Brebrick

H. CHEMICAL ANALYSIS

1. Wet Chemical Determination of Chromium, Magnesium, Titanium, and Nickel

Methods have been developed for determining chromium in chromium oxides and as an impurity in alumina (ruby). In both cases chromium is oxidized to the +6 state with ammonium persulfate and subsequently titrated with ferrous ammonium sulfate. The amount of chromium in the chromium oxides is large enough to be determined to an accuracy of within 2 parts per 1000, by using an automatic potentiometric method for finding the end point of the titration. In determining small quantities of chromium in alumina, the end point is obtained by an amperometric method. A hooked platinum electrode polarized at +1.0 volt is used as an indicating electrode and stirrer. The titration curve is plotted automatically, and the straight line portions are extrapolated in the conventional manner. Since the end point is found graphically, this method is slightly less precise than the potentiometric method, but it can be used in titrating solutions 10 to 1000 times more dilute.

In order to analyze $MgTiO_3$ for magnesium and titanium, methods based on EDTA titrations have been developed for determining these elements in the presence of each other. Magnesium is titrated directly in an NH_4OH-NH_4NO_3 pH 10 buffer, with triethanolamine used to mask Ti. The titration is performed automatically with the Reilley gold amalgam electrode.[21] The titanium

Fig. III-11. Mass spectrographic analysis of powdered MgTiO$_3$. Yields of magnesium and titanium ions in successive equal exposures.
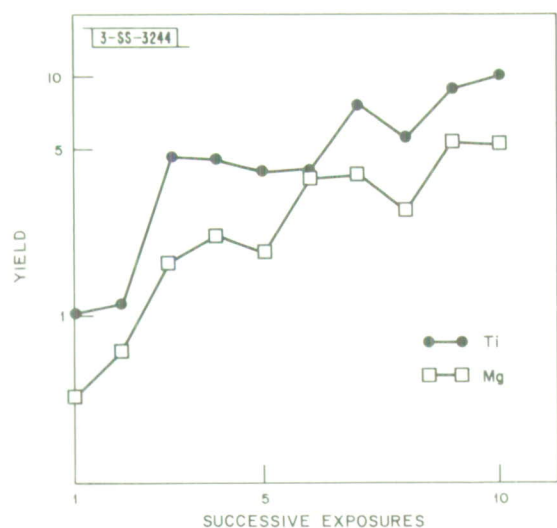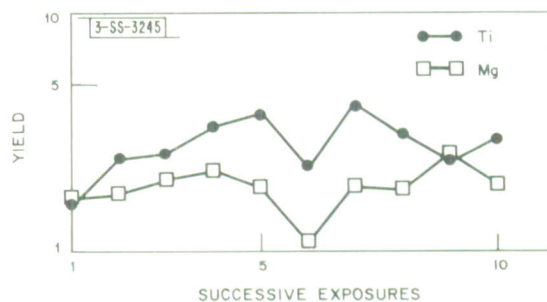
Fig. III-12. Mass spectrographic analysis of mixed MgO and TiO$_2$ powders. Yields of magnesium and titanium ions in successive equal exposures.
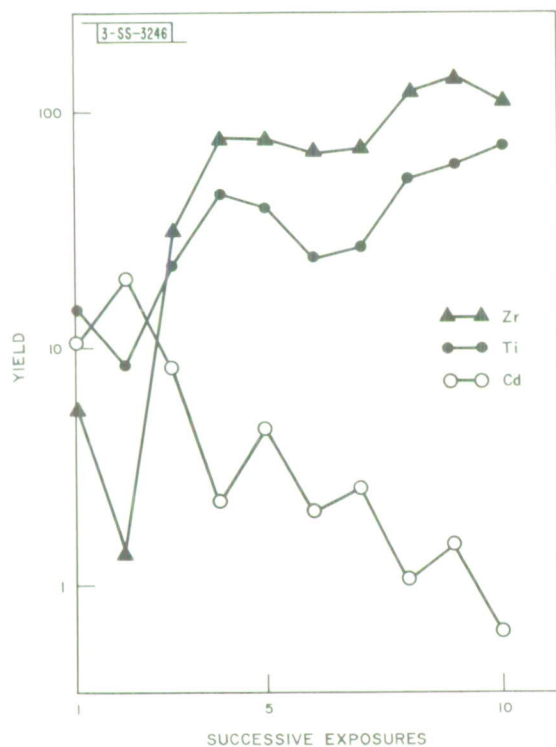

Fig. III-13. Mass spectrographic analysis of mixed CdO, TiO$_2$, and ZrO$_2$. Yields of cadmium, titanium, and zirconium ions in successive equal exposures.

determination employs a method[22] in which titanium is complexed with hydrogen peroxide, and excess EDTA is added to the peroxy complex buffered at a pH of 4.5 with sodium acetate-acetic acid. The excess EDTA is then back-titrated with a standard copper solution to a PAN end point. Because of the hydrogen peroxide added, the potentiometric end point is unsuitable.

Nickel in NiO has been determined to an accuracy of within 2 parts per 1000 by automatic potentiometric EDTA titration using the Reilley gold amalgam electrode.[21] The nickel is titrated directly in an NH_4OH-NH_4NO_3 pH 9 buffer.

<div align="right">M. C. Gardels
J. C. Cornwell</div>

2. Mass Spectrographic Analysis of Insulators

The technique described earlier[23] for mass spectrographic analysis of insulating materials, in which electrodes for use in the RF spark ion source are prepared by pressing a powdered mixture of the sample and graphite, is being investigated further. Preliminary data indicate that it is advantageous to substitute powdered silver metal for the graphite provided that silver of sufficient purity can be obtained. Because of silver's superior mechanical properties, the weight ratio of conductor-to-sample necessary to obtain electrodes of sufficient strength is smaller for silver than for graphite. For this reason, together with the greater atomic weight of silver, the total number of ions which must be produced in order to obtain a given number of sample ions is about 15 times greater for electrodes prepared with graphite than for those containing silver. Therefore, graphite electrodes require much more time for a given sample exposure, and the graphite must be 15 times as pure as the silver in order to achieve the same limit of detection.

Sufficiently soft insulators can be powdered in plastic vials with a shaking device ("Wig'L'Bug"). If the plastic contains no inorganic fillers, the only foreign lines introduced into the sample spectra by this procedure are due to hydrocarbons. The spectrograph has sufficiently high resolution to separate most of these from the lines due to the sample. Harder materials can be powdered by grinding with a steel mortar and pestle. If these materials are chemically inert, contamination from the steel can be dissolved away with suitable acids.

The effect of differences in sample volatility on analytical results has been investigated by determining the yields of various ions in ten, equal, successive exposures. Results of experiments on $MgTiO_3$, mixed MgO and TiO_2, and mixed CdO, TiO_2, and ZrO_2 are shown in Figs. III-11, III-12, and III-13, respectively. It is seen that the yield of cadmium ions decreased strongly with time because of the high volatility of CdO, but the relative yields of the other ions did not change appreciably.

<div align="right">E. B. Owens
N. A. Giardino</div>

REFERENCES

1. T.B. Reed, J. Appl. Phys. 32, 2534 (1961).

2. Y. Shimomura, M. Kojima, and S. Saito, J. Phys. Soc. Japan 11, 1136 (1956).

3. H. Lux and G. Illmann, Chem. Ber. 92, 2364 (1959).

4. D.C. Hilty, W.D. Forgeng, and R.L. Folkman, Trans. AIME 203, 253 (1955).

5. Solid State Research Report, Lincoln Laboratory, M.I.T. (1963:3), p. 25, DDC 427340.

6. Solid State Research Report, Lincoln Laboratory, M.I.T. (1963:4), p. 37.

7. R.E. Hanneman, M.D. Banus, and H.C. Gatos, J. Phys. Chem. Solids 25, 293 (1964).

8. P. Junod, Helv. Phys. Acta 32, 567 (1959).

9. Y. Baer, G. Busch, C. Frohlich, and E. Steigmeier, Z. Naturforsch 17a, 886 (1962).

10. P. Rahlfs, Z. Physik Chem. 31B, 157 (1963).

11. J.B. Conn and R.C. Taylor, J. Electrochem. Soc. 107, 977 (1960).

12. N.A. Goryunova, S.I. Radautsan, and G.A. Kiosse, Soviet Phys. — Solid State 1, 1702 (1960).

13. M.D. Banus, R.E. Hanneman, M. Strongin, and K. Gooen, Science 142, 662 (1963).

14. T.B. Reed, H.C. Gatos, W.J. LaFleur, and J.T. Roddy, Metallurgy of Advanced Electronic Materials, G.E. Brock, Ed. (Interscience, New York, 1963), p. 71.

15. J.C. Woolley, C.M. Gillett, and J.A. Evans, J. Phys. Chem. Solids 16, 138 (1960).

16. L.S. Brooks, J. Am. Chem. Soc. 74, 227 (1952).

17. L. Ch'un-hua, A.S. Pashinkin, and A.V. Novoselova, Russ. J. Inorg. Che. 7, 496 (1962).

18. R.F. Brebrick and A.J. Strauss, J. Chem. Phys. (in press).

19. Solid State Research Report, Lincoln Laboratory, M.I.T. (1962:4), p.29, DDC 400709. R.F. Brebrick and A.J. Strauss, J. Chem. Phys. (to be published).

20. G. Drummond and R.F. Barrow, Proc. Phys. Soc. (London) 65A, 277 (1952).

21. C.N. Reilley, R.W. Schmidt, and D.W. Lamson, Anal. Chem. 30, 953 (1958).

22. D.H. Wilkens, Anal. Chim. Acta 20, 113 (1959).

23. Solid State Research Report, Lincoln Laboratory, M.I.T. (1962:3), p. 11, DDC 291546.

IV. BAND STRUCTURE AND SPECTROSCOPY OF SOLIDS

A. COMPARISON OF MODELS FOR THE ELECTRON BANDS IN BISMUTH

The form of the dispersion relation $E(\vec{p})$ for electrons in bismuth has been the subject of considerable interest. In 1939, Shoenberg[1] proposed a simple parabolic-ellipsoidal model in which, in the principal axis system of the ellipsoid, the dispersion relation is given by

$$E(\vec{p}) = (\alpha_1 p_1^2 + \alpha_2 p_2^2 + \alpha_3 p_3^2)/2m \quad . \tag{1}$$

The values of the components of the reciprocal mass tensor $\overleftrightarrow{\alpha}$, which is diagonal in this system, are given approximately by[2]

$$\alpha_1 = 202 \quad , \quad \alpha_2 = 0.83 \quad , \quad \alpha_3 = 84.2 \quad . \tag{2}$$

This simple parabolic relation is expected to be valid only in the region where $E(\vec{p})$ is much less than the energy separation between the electron band and the other bands at the same point in the Brillouin zone. Lax, et al.,[3-6] observed that the electron bands in bismuth are, in fact, nonparabolic and proposed a nonparabolic-ellipsoidal dispersion relation which is given, again in the principal axis system, by

$$E(\vec{p}) \, [1 + E(\vec{p})/\epsilon_g] = (\alpha_1 p_1^2 + \alpha_2 p_2^2 + \alpha_3 p_3^2)/2m \quad . \tag{3}$$

The criteria for the validity of Eq. (3) are that the electron band interact strongly with only one other band, that the two bands have extrema at the same point in the Brillouin zone, and that all three principal components of $\overleftrightarrow{\alpha}$ are large. Cohen[2] has considered the possible forms which these dispersion relations may take depending on the location of the conduction band minima in the Brillouin zone. Since there is now considerable experimental[5,6] and theoretical[7] evidence that these minima occur at the centers of the pseudo-hexagonal faces of the Brillouin zone (L points), we consider only Cohen's case A which treats this situation. In Cohen's model, one assumes that a single valence band lies immediately below the electron band separated from it by a gap ϵ_g. All other bands are presumed to be far away so that interactions with them need be considered in lowest order only. One can then show that under the above conditions the dispersion relation can be written in the form

$$\frac{1}{\epsilon_g} [E(\vec{p}) - \frac{1}{2m} \vec{p} \cdot \overleftrightarrow{\alpha'} \cdot \vec{p}] \times [E(\vec{p}) + \epsilon_g + \frac{1}{2m} \vec{p} \cdot \overleftrightarrow{\alpha''} \cdot \vec{p}] = \frac{1}{2m} \cdot \vec{p} \cdot \overleftrightarrow{\alpha} \cdot \vec{p} \quad , \tag{4}$$

where $\overleftrightarrow{\alpha}$ represents the direct interaction with the valence band. The lowest-order effects of interactions with other bands and the contribution of the free-electron terms are contained in $\overleftrightarrow{\alpha'}$ and $\overleftrightarrow{\alpha''}$. Equation (4) represents the most general dispersion relation consistent with the assumptions made thus far. Since the experimental values of α_1 and α_3 in Eq. (1) are quite large, it is reasonable to assume that they arise primarily through a direct interaction between the two bands. Consequently, we can neglect these components in the $\overleftrightarrow{\alpha'}$ and $\overleftrightarrow{\alpha''}$ tensors so that Eq. (4) can be approximated in the principal axis system by

$$\frac{1}{\epsilon_g}\left[E(\vec{p}) - \frac{1}{2m}\alpha'_2 p_2^2\right] \times \left[E(\vec{p}) + \epsilon_g + \frac{1}{2m}\alpha''_2 p_2^2\right] = \frac{1}{2m}\left(\alpha_1 p_1^2 + \alpha_2 p_2^2 + \alpha_3 p_3^2\right) \quad . \tag{5}$$

Equation (5) is more general than either the two-band model proposed by Lax or the model proposed by Cohen. The two-band model can be obtained from Eq. (5) by setting $\alpha'_2 = \alpha''_2 = 0$. This amounts to completely neglecting the interactions with other bands as well as the free-electron contribution to the effective mass tensor. This is admittedly unjustified since the experimental value of α_2 is of the order of the free-electron contribution. Cohen's model, on the other hand, is obtained by setting $\alpha_2 = 0$, which amounts to neglecting this component of the velocity matrix element in the direct interaction between the two bands. Although experiment indicates that α_2 must be small, there is no a priori reason to assume that it is identically zero since there is no symmetry restriction of α_2 at the L point in bismuth. It may, in fact, be comparable to, or even larger than, α'_2 and α''_2. Hence, the α_2 term should not be neglected in Eq. (5). Therefore, we see that both the two-band model and the Cohen model involve approximations which are in some sense unjustified, and that a still more general dispersion relation [Eq. (5)] should be considered.

<div align="right">J. O. Dimmock</div>

B. MAGNETOREFLECTION EXPERIMENTS IN ANTIMONY[†]

Magnetoreflection studies are being carried out in antimony.[‡] The initial experiments involve the investigation of the effect of a magnetic field on the plasma structure of the optical reflectivity of antimony. Measurements have been carried out with the magnetic field parallel to the Poynting vector. When the magnetic field is directed along the binary direction, both plasma edges (one associated with E parallel to the bisectrix direction and one with E parallel to the trigonal direction) exhibit magnetic structures of similar shape, the former of much larger magnitude than the latter. When the magnetic field is directed along the trigonal direction, the single plasma edge also exhibits large magnetic structure.

Calculations of the magnetic field dependence of the optical reflectivity of antimony have been carried out on the basis of three tilted electron ellipsoids. This simple band structure model of antimony fails to give even qualitative agreement with the magnetoreflection experiment. We are now trying to explain the experimental results by including the effects of other carriers.

<div align="right">Mildred S. Dresselhaus
J. G. Mavroides</div>

C. DIAGRAMS FOR THE ANALYSIS OF FREE-CARRIER CONTRIBUTIONS TO THE DIELECTRIC CONSTANT IN A MAGNETIC FIELD

Several diagrams have been developed which are very helpful in analyzing experiments involving free-charge carriers in a magnetic field. For a lossless medium, the real part of the dielectric constant is given by $n^2 - k^2$, where $n - ik$ is the complex index of refraction. Then for propagation parallel to the magnetic field

$$n^2 - k^2 = \kappa' \left[\frac{\omega^2 - \omega\omega_c - \omega_p^2}{\omega(\omega \mp \omega_c)} \right] \quad , \tag{6}$$

and for propagation transverse to the field

$$n^2 - k^2 = \kappa' \left[\frac{\omega^4 - \omega^2(\omega_c^2 + 2\omega_p^2) + \omega_p^4}{\omega^2(\omega^2 - \omega_p^2 - \omega_c^2)} \right] \quad , \tag{7}$$

where $\omega_c = eH/m^*$, $\omega_p^2 = Ne^2/m^*\kappa'\epsilon_o$, and κ' is the dielectric constant of the lattice. Important optical phenomena will occur when $n^2 - k^2 = 0$, 1, and ∞. The first and third values represent the zeros and poles of the above expressions and can easily be shown on the diagrams of Figs. IV-1 and IV-2, where frequencies have been normalized to ω_p. A given experiment is analyzed by tracking its path on the diagram and inspecting the behavior of the index of refraction along the path.

As an example of the use of these diagrams, consider the analysis of a magnetoplasma reflection experiment where the magnetic field (ω_c/ω_p) is kept fixed and the incident frequency (ω/ω_p) is varied. The experimental path on the diagram of Fig. IV-1 is then a horizontal trace which we may choose to be $\omega_c/\omega_p = 1$ (for illustrative purposes). Recalling that the reflectivity R is given by $R = [(n-1)^2 + k^2]/[(n+1)^2 + k^2]$ and that for a lossless case $2nk = 0$, we see that in the crosshatched regions of the diagram $n = 0$, and $R = 100$ percent. In the clear regions of the diagram, $R = 0$ and $R = (n-1)^2/(n+1)^2$. As the frequency is decreased from $\omega/\omega_p = 3$ to zero (for example), the experimental point on the diagram will encounter decreasing n, and the
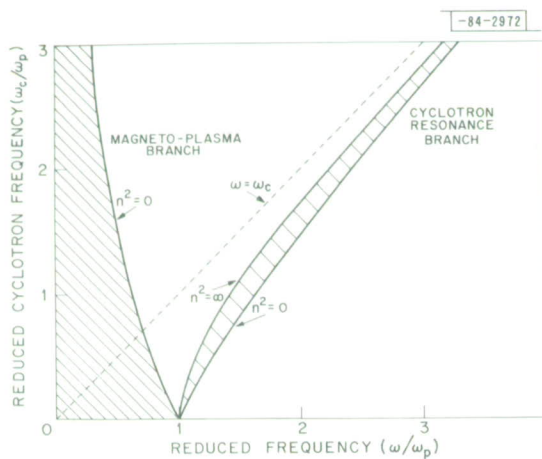

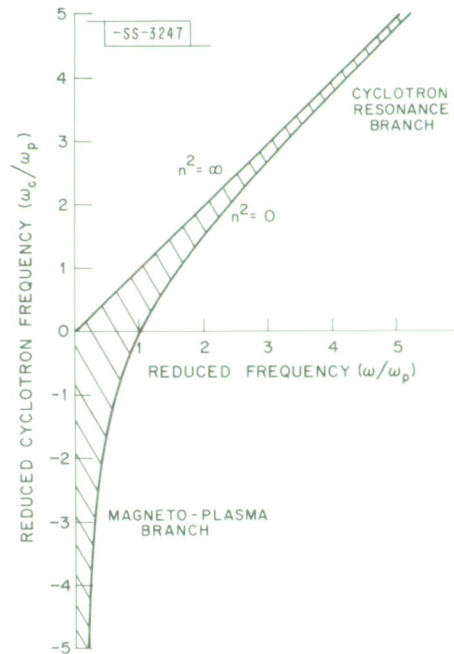Fig. IV-1. Poles and zeros of the dielectric constant for propagation transverse to the magnetic field.

Fig. IV-2. Poles and zeros of the dielectric constant for propagation parallel to the magnetic field.

43

reflectivity will decrease until n = 1 at which point R = 0. The index then decreases until n = 0 at which point R = 100 percent and remains so until $n^2 = \infty$. The reflectivity then decreases again and goes through the same cycle until it reaches 100 percent for the crosshatched region at the left. The first region of high reflectivity is the plasma-shifted cyclotron resonance; the second peak is the so-called magnetoplasma resonance branch. These diagrams clearly show the interrelation of cyclotron resonance, magnetoplasma reflection, and magnetoplasma resonance. They can also be used to discuss Faraday rotation, Voigt effect, helicon waves, and, in fact, all free-carrier magnetic effects in lossless media.

G. B. Wright

D. GALVANO-THERMOMAGNETIC EFFECTS IN HgSe

Using the dependence of energy on wave vector calculated by Kane[8] for InSb, six basic galvano-thermomagnetic transport coefficients (GTMTC) were derived in terms of specific transport integrals.[9] The transport integrals have now been evaluated numerically for parameters appropriate to HgSe at room-temperature, and various theoretical predictions have been compared with experiment. Since only a small number of theoretical parameters are involved and because a large number of effects are experimentally determined, the usual flexibility of adjusting parameters until theory and experiment are in accord is absent here. Nevertheless, the agreement between experiment and theory is exceedingly good. These results confirm the nonparabolic shape of the conduction band of HgSe and, furthermore, show that the dominant scattering mechanism for electrons in HgSe is polar scattering due to optical phonons.

T. C. Harman

E. MAGNETIC RESONANCE SATURATION IN CRYSTALS

We have considered the theory of magnetic resonance saturation in crystals as given by Provotorov[10] and found it wanting in some aspects.

First, the basic equation of his theory is dimensionally wrong. Although this does not affect his major conclusions for the steady state, it does make his expression for the function determining the linewidth and shape incorrect. Secondly, Provotorov's theory ignores "memory" effects which, although unimportant for the steady state in the rotating frame of reference, are quite important for the correct time evolution of the system and its approach to the steady state.

Some of these effects have been investigated by a technique analogous to the one proposed by Argyres and Kelley[11] and will be the subject of a future report. Recent experiments with the time evolution of the system indicate the desirability of such an investigation, as the experimental results are at variance with known theories.

P. N. Argyres

F. EFFECT OF IMPURITY ADDITIONS ON THE NERNST COEFFICIENT OF BISMUTH

The theory for the Nernst coefficient $H_y N_{zx}$ of bismuth in the high magnetic field region[12] shows that maximum values will occur for intrinsic material. Small additions of either p- or n-type impurities, i.e., lead or selenium, respectively, should reduce the magnitude but not change the sign of $H_y N_{zx}$. In order to check this theoretical prediction, impurities were added

TABLE IV-1
EFFECT OF ADDITION OF FOREIGN IMPURITIES ON THE NERNST COEFFICIENT OF PURE BISMUTH AT 85°K AND 5 kgauss

Impurity Added	Atomic Percent Added	Nernst Coefficient (μv °K^{-1})
none	-----	500
Lead	0.005	490
Lead	0.020	154
Lead	0.050	97
Selenium	0.010	90
Cadmium	1.0	182
Mercury	1.0	460

to bismuth during the single-crystal growth process. Measurements of $H_y N_{zx}$ at 5 kgauss and at 85°K were carried out. These data, along with the percent of impurity added, are presented in Table IV-1. In agreement with theory, it is seen that small additions of both n- and p-type impurities reduce the magnitude of the Nernst coefficient.

<div align="right">

T. C. Harman
S. Fischler
A. E. Paladino

</div>

REFERENCES

1. D. Shoenberg, Proc. Roy. Soc. (London) A170, 341 (1939); Progress in Low Temperature Physics, edited by C.J. Gorter (Interscience, New York, 1957), Vol. 2, Chap. 8.

2. M.H. Cohen, Phys. Rev. 121, 387 (1961).

3. B. Lax, J.G. Mavroides, H.J. Zeiger, and R.J. Keyes, Phys. Rev. Letters 5, 241 (1960).

4. B. Lax and J.G. Mavroides, Advances in Solid-State Physics, edited by F. Seitz and D. Turnbull (Academic Press, New York, 1960).

5. B. Lax, The Fermi Surface, edited by W.A. Harrison and M.B. Webb (Wiley, New York, 1960).

6. R.N. Brown, J.G. Mavroides, and B. Lax, Phys. Rev. 129, 2055 (1963).

7. A.L. Jain and S.H. Koenig, Phys. Rev. 127, 442 (1962).

8. E.O. Kane, J. Phys. Chem. Solids 1, 249 (1957).

9. T.C. Harman and J.M. Honig, J. Phys. Chem. Solids 23, 913 (1962).

10. B.N. Provotorov, Soviet Phys. — JETP 14, 1126 (1962).

11. P.N. Argyres and P.L. Kelley, Phys. Rev. (to be published).

12. T.C. Harman and J.M. Honig, J. Advances in Energy Conv. 3, 525 (1963).

V. MAGNETISM AND RESONANCE

A. THE SYMMETRY OF SPIN CONFIGURATIONS IN MAGNETIC CRYSTALS

Landau and Lifshitz[1] have shown (using symmetry arguments) that if a magnetic crystal undergoes a second-order phase transition at a magnetic-ordering temperature, the spin configuration of the ordered phase must transform as a basis function for a single irreducible representation of the crystallographic symmetry group of the paramagnetic phase. This places a definite restriction on the possible ordered spin configurations that can occur, without any assumptions concerning the specific interactions responsible for the magnetic ordering. Although this argument is rigorous only in the immediate vicinity of the transition temperature, it is satisfied at all temperatures in many crystals and appears to be violated only when a crystal undergoes a marked first-order phase transition or two separate phase transitions.

For the special case of Heisenberg exchange in the molecular-field approximation, the Landau-Lifshitz theory has been compared to the spin-configuration determinations of Kaplan, et al.,[2] and Bertaut.[3] It has been shown that in the high-temperature limit $T \lesssim T_N$, where T_N is the magnetic-ordering temperature; the method of Bertaut is rigorous and gives the same predictions as the Landau-Lifshitz theory. These two approaches thus have the same region of validity, and for this model they yield the same results. The difference between them lies in the fact that the general derivation of the Landau-Lifshitz theory does not require a specific form for the exchange energy; whereas Bertaut's method is based on a Heisenberg exchange. It has also been shown that the general group-theoretical methods of Landau and Lifshitz and of Bertaut cannot be employed in any rigorous solution of the ground-state problem. At low temperatures ($T \ll T_N$) the more specialized methods of Kaplan, et al., must be used.

The Landau-Lifshitz theory has been applied to zincblende β-MnS, where it is found that there is only one ordered spin configuration that is consistent with both the Landau-Lifshitz theory and the neutron-diffraction results. This is the spiral structure with a 90° turn angle that has been proposed by Keffer[4] on other grounds. This demonstrates, in part, the usefulness of the general group-theoretical methods.

The Landau-Lifshitz theory is not restricted to crystals having localized atomic moments. Pickart, et al.,[5] have found that in the temperature interval $T_s < T \lesssim T_N$, where T_s is the spin-flip temperature, the spin density of α-Fe_2O_3 is not centered on the iron-atom positions. Therefore, to further illustrate the usefulness of the Landau-Lifshitz approach the general spin-density function of high-temperature ($T_s < T \lesssim T_N$) α-Fe_2O_3 has been considered. The most general function with the proper transformation properties has very little symmetry and possesses not only a generalized antiferromagnetic component in the (111) plane, but also a generalized Dzyaloshinsky component perpendicular to it [also in the (111) plane]. The spatial distribution of these two components is not required by symmetry to be the same and may be quite different. The result is compatible with Kaplan's[6] theoretical interpretation of the neutron data, which is based on a ligand-field approach.

Dzyaloshinsky[1] has also applied the Landau-Lifshitz theory to the low-temperature ($T < T_s$) magnetic phase of α-Fe_2O_3. Since he used the symmetry group of the paramagnetic phase for this, the argument is not legitimate. This point is made in order to emphasize the limitations of the Landau-Lifshitz theory.

J. O. Dimmock

B. MAGNETIC PROPERTIES OF $CoCr_2O_4$

1. Magnetic Resonance

Measurements of magnetic resonance as a function of temperature have been made on small, single-crystal samples of ferrimagnetic $CoCr_2O_4$ using millimeter spectrometers from 24 to 135.5 kMcps. Over the temperature range from liquid helium to the Curie temperature of 98°K, two distinctive types of resonances were observed. One, the uniform-mode resonance, consisted of a number of relatively weak satellite lines grouped about a stronger line near the paramagnetic resonance field value. The second type, consisting of a strong, broad resonance that varied considerably in field with temperature, has been identified tentatively as a modified exchange mode (see Sec. B-2).
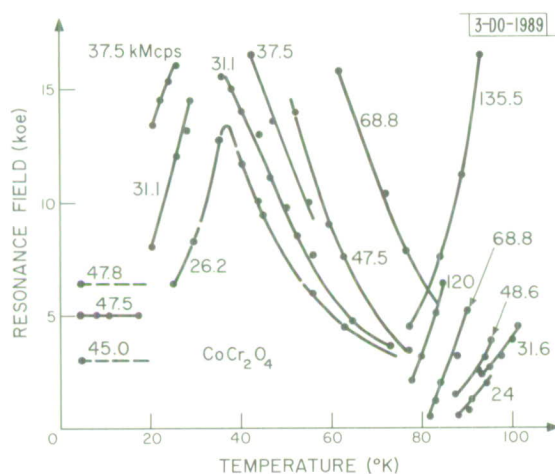

Fig. V-1. Field for resonance in "modified exchange mode" of $CoCr_2O_4$ as a function of temperature, at a number of microwave frequencies.

Figure V-1 shows the measured resonance field at different frequencies as a function of temperature for the exchange mode. Near 20° and 77°K, the resonance field was observed to change discontinuously resulting in three different temperature regions of magnetic resonance. From 4.2°K to the first transition temperature near 20°K (Region 1), the resonance field was constant; from approximately 20° to 77°K (Region 2), the resonance field varied with temperature giving a sharp peak in field near 35°K; from approximately 77° to 100°K (Region 3), the resonance field increased uniformly with temperature. Except for the discontinuous change in the resonance field near 20° and 77°K, the resonance field appeared qualitatively to vary in an inverse manner with the static magnetization over the temperature range of 35° to 98°K. The resonance absorption was always observed to be strongest near the low-field values and broadened and decreased in intensity at higher fields.

Fig. V-2. The spin resonance spectrum in the "uniform mode" of CoCr₂O₄ as a function of magnetic field at 18° and 53°K.
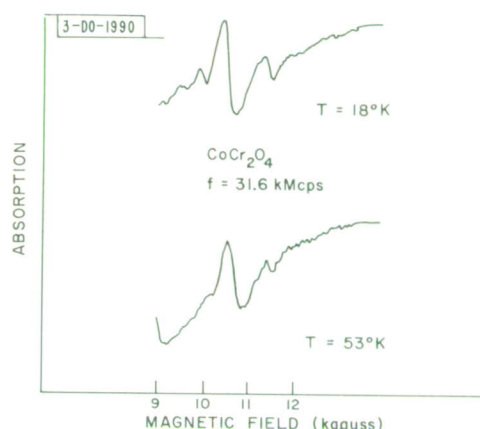
Figure V-2 shows recorder traces of the uniform resonance mode taken at two different temperatures using field modulation. At least four distinct satellite resonances were observed on the main uniform precession mode at helium temperatures. At higher temperatures (near 40° to 50°K) the weaker resonances had faded, leaving only the main uniform-mode resonance and one satellite line still visible.

There seems to be a remarkable qualitative correlation between the spin resonance observations and the results of theoretical calculations and other experimental observations of $CoCr_2O_4$. Theoretical calculations (see Sec. B-2) indicate that, coming down in temperature, the spin system should first order in a Néel configuration down to ~87°K. This is observed in neutron diffraction and seems to correlate with Region 3 in the exchange-mode data. Below ~87°K the theory indicates that the structure should be an ordered spiral, but no transverse-correlated spin moment is detected just below this temperature in the neutron-diffraction results. This transition in the theory seems to correlate with the transition to Region 2 of the exchange-mode data. Finally, at ~30°K and below, the neutron data appear to show the onset of a correlated transverse moment, even though the theory indicates no unusual change below this temperature. This onset of transverse correlation seems to correlate with Region 1 of the exchange-mode data.

The occurrence of satellites on the uniform-mode line also may be related to the presence of a spiral-spin structure. The fading of the satellite structure as the temperature rises toward the transition to the Néel state could then reflect the gradual loss of transverse-spin correlation.

The analysis of the exchange-mode resonance will require a theoretical examination of the mode spectrum of the spin system over the entire range of observed temperature. The simplest case to analyze should be the Néel region, where two exchange modes could occur. One of these modes will have resonance frequency given by (see Sec. B-2)

$$\omega = \left| -\gamma H + \gamma \lambda \left[M_A(H, T) + \bar{u} M_B(H, T) \right] \right| \quad , \tag{1}$$

where $\lambda = 12 J_{AB}/\gamma^2$. If the sublattice magnetizations have a large susceptibility in Region 3 (magnetization measurements show such a susceptibility) and if the change in the M's is assumed linear in H, we have

$$\omega = \left| \gamma \{ \lambda \left[\chi_A(T) + \bar{u} \chi_B(T) \right] - 1 \} H + \gamma \lambda \left[M_A(O, T) + \bar{u} M_B(O, T) \right] \right| \quad ,$$

49

where

$$M_A(H, T) = M_A(O, T) + \chi_A(T) H \quad ,$$

$$M_B(H, T) = M_B(O, T) + \chi_B(T) H \quad .$$

To interpret the observed variation of resonance field with T and ω in Region 3, in terms of the exchange mode of Eq. (1), this crude argument indicates that $\lambda [\chi_A(T) + \bar{u}\chi_B(T)]$ must be positive and have a value larger than one.

It is not yet entirely clear why the presence of a spiral-spin configuration should produce satellite lines on the uniform mode. One possible explanation of this is that the spiral structure is not a pure k_o spiral, but has weak sidebands at k-values $k_o \pm nk'$ near k_o. This allows coupling of the microwave field, not only to the uniform mode of precession, but also to spin waves of k-vector $k_o \pm nk'$.

There remains the question of what produces the weak sidebands on the spiral k-vector k_o. One possibility is that these sidebands are produced in domain walls, where the direction of propagation of k_o changes; the satellite structure would then depend on the presence of a cor-related transverse spiral structure and be due to resonance in domain walls.

<div align="right">

J. J. Stickler
H. J. Zeiger

</div>

## 2. Preliminary Considerations of Electron Resonance in Cubic Spinels with Spiral-Spin Configurations

According to our previous studies,[7-9] cobalt chromite is a (classical) Heisenberg ferri-magnet. That is, our measurements (at 4.2°K) of its magnetization and neutron diffraction patterns, together with their successful interpretation in terms of spin-only ionic moments and a spiral-spin configuration, were consistent with this primary assumption. Furthermore, the measured paramagnetic diffuse-neutron scattering above its Curie point of 96°K was consistent with the rigorous high-temperature Heisenberg expansion. In addition, its magnetic anisotropy appeared to be small so that no other forces were obviously significant.

Given the assumption of the Heisenberg Hamiltonian, the only parameters are the exchange integrals (or ratios thereof). It was convenient to make a secondary assumption as to which of these are significant; therefore we assumed that cobalt chromite possessed only nearest-neighbor A-B and B-B interactions. Except possibly for a 5-percent error in the length of the spiral propagation vector, our 4.2°K data were consistent with this additional assumption and yielded $u = 2.00 \pm 0.08$, where $u = (4/3) (J_{BB}/J_{AB})$. In addition, the remaining parameter J_{AB} has been estimated from the Curie point to within, perhaps, ± 10 percent by using the rigorous, high-temperature expansion. Thus, appropriate values for both of the parameters involved in our model for cobalt chromite have been uniquely determined.

We then used the molecular-field approximation to compute the thermal averages of the spins at finite temperatures, from the inflexible model predetermined above. The resulting calculated values for the magnetization as a function of temperature (with the customary renormalization to the experimental Curie point and with $u = 2.03 \pm 0.03$) were in remarkably close agreement with our actual measurements on cobalt chromite. This agreement was interpreted as a clear

affirmation of the accuracy of the molecular-field approximation, particularly since its net magnetization consists of a small difference between large sublattice magnetizations over its entire ferrimagnetic temperature range. Thus, we concluded that the ferrimagnetism of cobalt chromite is associated with one of three different types of ordered states (depending on the temperature) as indicated in Fig. V-3. (There is collinear Néel configuration from T_c to T_2, spiral from T_2 down to T_1, and presumably a modified spiral below T_1.)

Fig. V-3. Experimental and theoretical variation of magnetization with temperature for cobalt chromite. The two transition temperatures are indicated as T_1 and T_2.
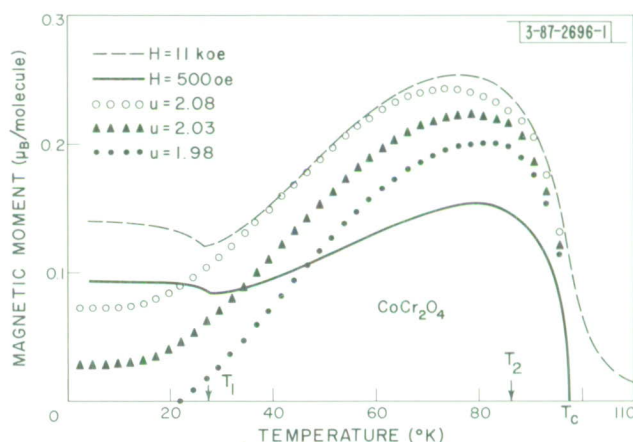
However, the azimuthal components in the molecular-field, spiral-spin configuration discussed above would give rise to sharp satellite peaks in its neutron diffraction pattern from 0°K to T_2, whereas, experimentally, such peaks were found to exist only from 0°K to T_1', which is only slightly above T_1. The standard interpretation of this neutron diffraction result required that the average spin vectors in cobalt chromite be collinear between T_1' and T_2. Nevertheless, the diffraction peaks predicted from the axial components of the molecular-field spins were in excellent agreement with experiment. Thus we were faced with the fascinating question of why the apparent accuracy of the molecular-field approximation should be different for the axial and azimuthal components of the average spins. In addition, there was uncertainty as to what constituted the "best" description of the ordered state of cobalt chromite between T_1 and T_2.

Recently magnetic resonance absorption experiments have been performed[10] on single crystals of $CoCr_2O_4$ (see Sec. B-1). Besides the usual uniform mode with frequency $\omega = g\mu_B H$ (g was found to be very close to 2), other modes were found which showed very unusual temperature variations. Referring to Fig. V-1, which shows resonance field vs T, we see a great deal of structure to the curves. This suggests that a detailed theoretical understanding of these resonance properties will add considerably to our understanding of the physics of the spin system. One can even hope that some light will be thrown on the interesting conceptual problem discussed above. We shall discuss here some of our preliminary considerations on the theory of the resonance behavior.

First, referring to Fig. V-1 for $H_{res}(T)$, we see a general qualitative correlation with previous results. There are two temperatures, $\tau_1 \approx 20°K$ and $\tau_2 \approx 75°$ to $90°K$, at which H_{res} seems to suffer a discontinuity. The lower temperature seems to be correlated with either the kink in the magnetization curve [M(T) of Fig. V-3] or the temperature below which long-range

spiral peaks (satellites) occur. (Whether or not the two latter temperatures are actually distinct is experimentally uncertain at present.) Particularly interesting is the discontinuity in $H_{res}(\tau)$ at τ_2, where neither the neutron diffraction intensities nor $M(T)$ shows anything discontinuous. However, the molecular-field approximation does predict a transition at $T_2 \cong 87°$, below which the transverse or spiral-spin components increase rapidly (with an infinite initial slope).

To investigate this further we consider the resonance frequencies for the temperature range $T_2 - T_c$, where both the molecular-field approximation and the neutrons say that the ordering is a simple Néel state. We follow the standard procedure, which has worked well in the past, for the calculation at $T > 0$. The spin-wave equations of motion are used, but the spin quantum numbers are replaced by the thermal-averaged spins at temperature T. (This is also what is done in the random phase approximation.) These have already been worked out.[11] For our model of near-neighbor AB and BB interactions and equal g-factors, the three lowest frequencies are given by

$$\hbar\omega_o = \gamma H \qquad , \qquad \text{uniform mode}$$

$$\hbar\omega_u = \left| \gamma H - 12 J_{AB} \frac{M^*}{\gamma} \right| \qquad , \qquad \text{"u" mode}$$

$$\hbar\omega_e = \left| \gamma H - 12 J_{AB} \frac{M}{\gamma} \right| \qquad , \qquad \text{"exchange" mode} \qquad ,$$

where $\gamma = g\mu_B > 0$ ($g \cong 2$),

$$M = M_A + M_B \qquad ,$$

$$M^* = M_A + \bar{u}M_B \qquad ,$$

$$\bar{u} = \frac{2}{3} \frac{J_{BB}}{J_{AB}} \qquad .$$

For $CoCr_2O_4$ ($S_A = S_B$):

$$\bar{u} = 0.5\,u = 1.01 \pm 0.02 \qquad ,$$

as already discussed; M_A and M_B are the z-components of the sublattice magnetizations per molecule; and H (≥ 0) is the external field in the z-direction. With an eye toward the temperature region $T_1 < T < T_2$, we note that the above expressions are also valid for a pseudo-Néel ordering, where there are two different B-site magnetizations.

As we have said, ω_o has been observed and behaves properly. Ordinarily ω_e and ω_u would be very high (infrared). However, M and M^* are both an order of magnitude smaller than usual ($M \approx 0.1\,\mu_B$ while M_A and $M_B \approx 1\,\mu_B$), so that we can hope that ω_e or ω_u can be identified with the complicated resonance of Fig. V-1. Before discussing numbers further, we first note an important qualitative fact. There is good evidence[8] that the A-sites dominate, i.e., $M_A > 0$, $M_B < 0$, and $M > 0$. It also turns out that $M^* > 0$. Hence, naively, the above expressions say that H_{res} should be linear in M or M^* with positive coefficient and, therefore, H_{res} should decrease with increasing T for $T > T_2$ (contrary to Fig. V-1). However M and M^* depend on H; writing

$$M = M_O + \chi H \quad , \qquad M^* = M_O^* + \chi^* H \quad ,$$

with M_O and M_O^* defined as the values for $H = 0$, we have

$$\hbar\omega_e = \left| \gamma \left(1 - \frac{12\,J_{AB}\chi}{\gamma^2} \right) H - 12\,J_{AB}M_O \right| \equiv \left| \gamma_{eff}H - 12\,J_{AB}M_O \right|$$

and, similarly, for ω_u. A rough estimate [obtained from the results of Ref. 8 in which M(T) was measured in 1/2 and in 10 kgauss] gives $\chi \sim 0.003$ to $0.01\,\mu_B$/kgauss. Using the result for $CoCr_2O_4$, $T_c/T_M \cong 0.5$ (T_c = Curie temperature, T_M = Curie temperature in the molecular field approximation[12]) which is derived from the first three terms in the sequence defined by the Kramers-Opechowski method, and using the experimental value $T_c = 96°K$, we obtain $J_{AB} \cong 1.2 \times 10^{-3}$ ev and

$$12\,J_{AB}\chi/\gamma^2 \cong 2 \text{ to } 6 \quad .$$

Thus, we can expect $\gamma_{eff} < 0$ so that H_{res} should increase as M_O decreases, i.e., as T increases above T_2 (in agreement with data presented in Fig. V-1). Also note that γ_{eff} depends on H and T. Our mechanism for this dependence is different from that discussed by Wangsness,[13] where H, T dependence results from inequality of the various g-factors. We expect the latter effect to be relatively small in these materials.

Despite this good qualitative beginning, there is a difficulty which appears to be serious. Referring to Fig. V-1, we see that a zero-field resonance is indicated at $T \sim 80°$ to $90°$, $\nu \approx 30$ kMcps. We have for $H = 0$ (from our formula), as given above,

$$\nu_e = \omega_e/2\pi = \frac{12\,J_{AB}}{h\gamma} M_O = 1800\,M_O \text{ kMcps} \quad (M_O \text{ in Bohr magnetons}) \quad .$$

At $T = 86°K$, $M_O = 0.208\,\mu_B$ (giving $\nu_e = 372$ kMcps). To compute M_O^*, we use $M_A = 1.60\,\mu_B$ and $M_B = -1.39\,\mu_B$ as given by the molecular-field approximation (which gives very close agreement with the neutron-diffraction intensities); with $\bar{u} = 1.01$, we find $\nu_u = 347$ kMcps. Thus the calculated frequencies are more than an order of magnitude too large.

There are at least two possible sources of this discrepancy. The first is the error introduced in the standard theory of resonance. (The reason for this error is that it involves the replacement in the equations of motion of thermal averages of spin products by products of average spins.) The second is error due to the basic simplified model (which neglects all forces except the nearest-neighbor A-B and B-B isotropic exchange interactions). The latter error might be important in view of the high sensitivity of ν_u to changes in $\bar{u}$, i.e., it is seen from the numbers above that a 1-percent increase in $\bar{u}$ gives a 7-percent decrease in ν_u, alternately, an increase of only 15 to 20 percent in $\bar{u}$ is sufficient to decrease ν_u by the required order of magnitude. Such a change in $\bar{u}$ is far outside the experimental limits within the model previously studied. However a change in the model to include second-neighbor B-B exchange interactions, for example, gives rise to formulas for the ω's of the same form as given above with a new parameter $\bar{u}'$ simply replacing $\bar{u}$. It must be remembered that these extra interactions will also have an effect on the magnetization and the magnetic ordering as seen by neutrons, so that their choice will be severely limited by the extensive agreement with experiment previously obtained.

Because of these discrepancies, both in the resonance and in the neutron diffraction experiments, there are a number of experiments and calculations that obviously should be performed. We are continuing these investigations.

T. A. Kaplan
K. Dwight
N. Menyuk

C. COMPOUNDS WITH B31 $\rightleftharpoons$ B8$_1$ TRANSITIONS

1. X-Ray Studies

In order to investigate our earlier proposal that the phase transitions found in MnAs are due to partial spin quenching, we have been studying the crystallographic and magnetic properties of MnAs-MnP and MnAs-MnSb.

MnAs has the B8$_1$ (or NiAs) structure at all temperatures except the interval 40°C < T < 140°C, where it has the B31 (distorted NiAs of MnP) structure. With antimony substitutions, the high-temperature transition is lowered, the B31 temperature interval disappearing near 15 atomic percent MnSb. With phosphorus substitutions, the high-temperature transitions show an initial decrease (to ~3 atomic percent MnP) and then a steady increase. The low-temperature transition remains roughly constant with antimony additions, but shows a decrease of about 15°C by two atomic percent MnP. For $\geqslant$4 atomic percent MnP, there is no low-temperature transition — the B31 distortion continuing to increase with decreasing temperature to the magnetic ordering temperature and remaining to lowest temperatures. These results, and our initial magnetic measurements, are compatible with spin quenching in the B31 phase that increases with decreasing temperature to the Curie temperature.

D. H. Ridgley
W. A. Newman
J. B. Goodenough

2. Chemical Analyses

Considerable effort has been required to develop analytical procedures that are satisfactory for the MnAs-MnP and MnAs-MnSb systems. Standard chemical analysis methods for the ions involved are either not sufficiently accurate or cannot be applied in standard form because of interference by other ions present.

After trials with a number of variations on the standard bismuthate method for manganese, a procedure has been developed which yields an accuracy of 0.1 to 0.2 percent of the manganese present. The problem of chemical similarities of phosphorus, arsenic, and antimony has not been completely overcome and satisfactory results have been achieved in the case of phosphorus with arsenic only. A method which allows for the presence of antimony is under study.

The procedure used for arsenic with phosphorus is as follows: dissolve the sample in bromic acid, reduce the arsenic with stannous chloride, remove excess stannous ion with mercuric chloride, reoxidize with standardized permanganate solution. Phosphorus is determined by precipitation as magnesium ammonium phosphate followed by reprecipitations for purification. This procedure for phosphorus is accurate to approximately 2 percent but is satisfactory with small amounts of phosphorus. Arsenic has been determined by the above method to an accuracy of 0.2 percent in known materials.

One composition in the MnAs-MnP system has been completely analyzed using the procedure just discussed. The composition sought in preparation was $MnAs_{0.95}P_{0.05}$; the analyses showed $MnAs_{0.947}P_{0.047}$.

D. H. Ridgley
E. Whipple

D. EFFECT OF Mn^{3+} ON CATION ORDERING IN LITHIUM SPINELS

Numerous spinels containing B-site lithium have been found (by x-ray diffraction) to possess a superstructure similar to that originally reported for lithium ferrite, $Fe[Li_{0.5}Fe_{1.5}]O_4$.[14] Whereas the spinel lattice is normally face-centered cubic, the symmetry in these lithium spinels is found to be primitive. This indicates an ordering of the lithium ions on the occupied octahedral sites. The variety of lithium spinels of this type appeared to indicate that such ordering occurs whenever one-quarter of the B-sites are occupied by Li^+, the other B-sites by M^{3+} or M^{4+}. However, we have recently found that substitution of Mn^{+3} for Fe^{+3} on only 15 percent of the octahedral sites destroys completely the superstructure in $Li_{0.5}Fe_{2.5}O_4$. Since Mn^{+3} is a Jahn-Teller ion known to induce a tetragonal distortion in the spinel lattice at B-site concentrations $\gtrsim 60$ percent, it was felt that the disordering tendency might be associated with the Jahn-Teller effect even though the concentration is much too small to induce a long-range cooperative distortion. The effect may be related to the empirical observation that about 20 to 25 percent occupancy of the spinel B-sites by a Jahn-Teller ion gives maximum B-H loop squareness for computer memory cores.

We have begun an investigation to determine both the uniqueness of Jahn-Teller ions in inhibiting B-site ordering in lithium spinels and the critical concentration of these ions. The ordered spinel $Li_{0.5}Ga_{2.5}O_4$ was selected as a reference base for substitutions because gallium is primarily trivalent; the question of valence states is thus precluded. Trivalent chromium and rhodium, in addition to Mn^{+3}, have been substituted into the gallate base in order to demonstrate that the effect is not due merely to charge density on the Mn^{+3}.

Table V-1 summarizes the results found to date. For comparison, several ordered spinels reported by other authors are included in the table. It can be seen that Mn^{+3} is unique (among the B-site ions in the table) in its ability to destroy the lithium ordering.

R. W. Germann
R. J. Arnott
D. B. Rogers

E. SINGLE-CRYSTAL GROWTH OF VANADIUM SPINELS BY ELECTROLYTIC REDUCTION

Considerable progress has been made in the growth of single-crystal vanadium spinels by electrolytic reduction from fluxes. Work thus far has centered on the cobalt spinel system, CoV_2O_4-Co_2VO_4, which is of greater interest and, at the same time, chemically more difficult than the other vanadium spinels.[17] It is believed that if the experimental techniques for growing the cobalt system are worked out, the remaining members of the vanadite series will follow easily.

We have found that reduction of pentavalent vanadium in the presence of Co^{+2} leads to the precipitation of $Co_{1+x}V_{2-x}O_4$ ($0 \leqslant x \leqslant 1$) from fluxes of Na_2WO_4-WO_3. The value of x is

TABLE V-1			
MIXED SPINELS CONTAINING LITHIUM			
Formula	Lattice Parameter (Å)	Remarks	Reference
$Li_{0.5}Fe_{2.5}O_4$		with superstructure	14
$Li_{0.5}Ga_{2.5}O_4$	8.21	with superstructure	15,[†]
$Li_{0.5}Al_{2.5}O_4$	7.93	with superstructure	15
$LiMg_{0.5}Ti_{1.5}O_4$	8.37	with superstructure	16
$LiCo_{0.5}Ti_{1.5}O_4$	8.36	with superstructure	16
$LiCu_{0.5}Ti_{1.5}O_4$	8.34	no superstructure; 15% B-sites contain lithium	16
$Li_{0.5}Ga_{2.2}Cr_{0.3}O_4$	8.20	with superstructure	[†]
$Li_{0.5}Ga_{2.2}Rh_{0.3}O_4$	8.20	with superstructure	[†]
$Li_{0.5}Ga_{2.2}Mn_{0.3}O_4$	8.26	no superstructure	[†]
$Li_{0.5}Ga_{2.25}Mn_{0.25}O_4$	≈8.20	superstructure, but weak	[†]
$Li_{0.5}Ga_{2.3}Mn_{0.2}O_4$	≈8.18	with superstructure	[†]

† This work.

dependent upon the basicity of the flux mixture which, in turn, is determined by the ratio of the Lewis base, Na_2WO_4, to the Lewis acid, WO_3.

Initial attempts to grow single crystals by this technique were made using a ceramic double-cell of the type described in the last Solid State Research report (1963:4). It was found, however, that considerable contamination of the product with magnesium from the MgO crucible occurred. Also, the temperature at which the electrolysis could be conducted was limited by the increasing rate of reaction between the flux and the ceramic cell. In order to avoid these difficulties the platinum double-cell, shown in Fig. V-4, has been constructed. This device is similar to the ceramic cell, except that reduction occurs in the inner chamber. A platinum barrier is hung from the inner crucible by a platinum screen, in order to exclude oxygen formed at the anode from entering the cathode chamber. The initial cost of such a cell is considerably higher than that of a ceramic cell, but it has the advantages of being reusable and is considerably more versatile. The platinum double-cell has been used under conditions of low current density to grow crystals of several compositions in the CoV_2O_4-Co_2VO_4 system under flowing nitrogen. These conditions are listed in Table V-2.

The approximate composition shown in Table V-2 is based on an analysis for total reducing power of the vanadium in each sample. The maximum size of the crystals obtained thus far is about 3 to 4 mm. We are presently conducting experiments to determine the minimum value of x obtainable from the tungstate fluxes. Since the product crystals are excellent electrical conductors, the use of these as seeds should make possible the growth of crystals of any desired size.

The last row in Table V-2 gives the results of a single run using a borax-sodium fluoride flux suggested by Andrieux and Bozon.[18] Using considerably lower current density than they,
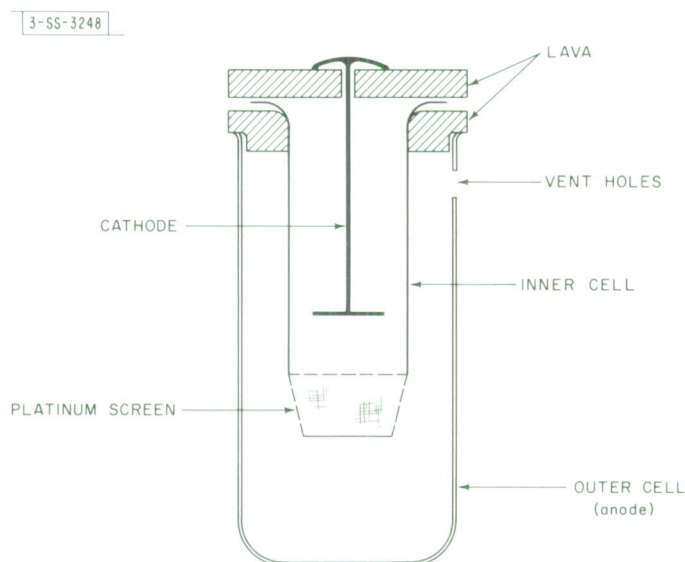

Fig. V-4. Platinum double-cell.

57

|				
TABLE V-2				
EXPERIMENTAL CONDITIONS FOR GROWTH OF VANADIUM SPINELS BY FUSED SALT ELECTROLYSIS				
Flux Composition	Current Density (ma cm^{-2})	Temperature (°C)	Duration of Electrolysis (days)	Approximate Product Composition
$1CoO:1V_2O_5:0.72WO_3:2.78Na_2WO_4$	~130	800	3	$Co_{1.54}V_{1.46}O_4$
$1CoO:1V_2O_5:0.4WO_3:3.6Na_2WO_4$	~20	900	10	$Co_{1.38}V_{1.62}O_4$
$1CoO:1V_2O_5:0.2WO_3:3.8Na_2WO_4$	~100	900	1	$Co_{1.22}V_{1.78}O_4$
	~10	900	7	
$1Na_2B_4O_8:0.5NaF:0.11V_2O_5:0.5CoO$	250	920	8	see p. 59
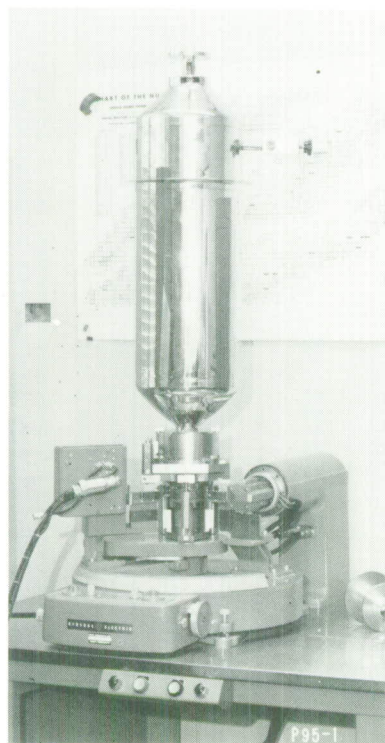
Fig. V-5. Helium dewar.

and the platinum double-cell just described, we obtained numerous well-formed spinel octa-hedra. However, the major phase present consisted of crystal rods (up to about 5 mm in length) which appear to have a crystal structure related to the mineral ludwigite. This would correspond to an approximate formula Co_2VBO_5. These rod-like crystals appeared to be formed on the inner cell walls and may have precipitated from solution upon cooling. With proper adjustment of the experimental conditions, the use of borate fluxes appears to provide an alternate to the tungstates for vanadite crystal growth. Work on these problems is continuing.

D. B. Rogers
A. Ferretti
E. J. Delaney

F. LOW-TEMPERATURE X-RAY DIFFRACTION

The construction of the low-temperature apparatus is almost completed. Figure V-5 shows the helium dewar mounted on the orienting mechanism and installed on the General Electric Co. diffraction unit. It seems to be satisfactory except that the sample base has a strong tendency to vibrate when jarred. Shock-mounting of the entire unit may solve this. Only a sample holder remains to be constructed.

R. J. Arnott
A. Ferretti

G. PHONON ATTENUATION IN QUARTZ AT 70 kMcps

Considerable improvement in both the number and amplitude of longitudinal phonon echoes in x-cut quartz has permitted measurement of the relative phonon attenuation, using the first five echoes, over the temperature range from 4.2° to 30°K. Figure V-6 shows an echo display that is typical of the best that has been obtained so far. The sample was prepared so that the best quality surface possible (roughness <1 micro-inch) would be produced.

The improved attenuation curve is shown in Fig. V-7. The accuracy is limited primarily by the large (~ 4 db) decrement between successive echoes. The decrement limits the number
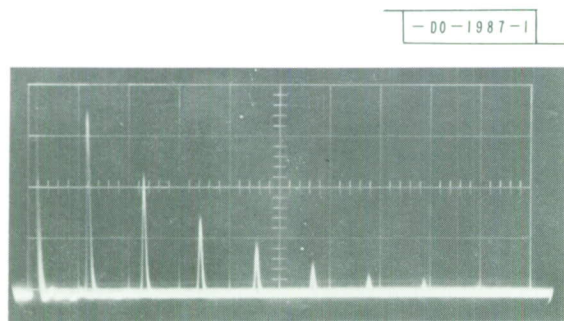

Fig. V-6. Longitudinal phonon echoes excited in a 1/4-inch-long, x-cut quartz rod placed in a micro-wave cavity. Horizontal scale is 2 μsec per division.
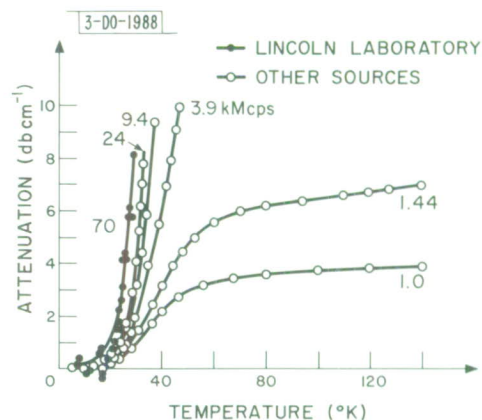

Fig. V-7. Temperature dependence of relative attenuation of longitudinal phonon echoes in x-cut quartz at 70 kMcps. The other curves, shown for comparison, are taken from the literature. All curves normalized to zero db cm^{-1} at 4.2°K.

of observable echoes, especially at the higher temperatures. The large decrement is attributed to surface roughness and interference effects.

Employment of a pulse integrating technique has resulted in an improvement of signal-to-noise ratio of ~ 10 db over the oscilloscope display measurement. With this method the first echo has been measured over a 30-db range or, equivalently, a maximum change in relative attenuation of over 30 db cm^{-1} has been determined.

J. B. Thaxter
P. E. Tannenwald

REFERENCES

1. L. D. Landau and E. M. Lifshitz, Statistical Physics (Addison-Wesley, Reading, Mass., 1958), Chap. 14. See also I. Dzyaloshinsky, J. Phys. Chem. Solids 4, 241 (1958); J. O. Dimmock, Phys. Rev. 130, 1337 (1963).

2. T. A. Kaplan, Phys. Rev. 116, 888 (1959); T. A. Kaplan, Phys. Rev. 119, 1460 (1960); D. H. Lyons and T. A. Kaplan, Phys. Rev. 120, 1580 (1960); D. H. Lyons, T. A. Kaplan, K. Dwight, and N. Menyuk, Phys. Rev. 126, 540 (1962).

3. E. F. Bertaut, Magnetism, G. T. Rado and H. Suhl, Eds. (Academic Press, New York 1963), pp. 149-209 and references contained herein.

4. F. Keffer, Phys. Rev. 126, 896 (1962).

5. S. J. Pickart, R. Nathans, and H. A. Alperin (to be published).

6. Solid State Research Report, Lincoln Laboratory, M. I. T. (1963:4), p. 63.

7. D. H. Lyons, T. A. Kaplan, K. Dwight, and N. Menyuk, Phys. Rev. 126, 540 (1962).

8. N. Menyuk and K. Dwight, J. Phys. radium (to be published).

9. The work on $MnCr_2O_4$ of J. Hastings and L. Corliss, Phys. Rev. 126, 556 (1962) is closely related. However, to be specific, we will confine our discussion here to $CoCr_2O_4$.

10. Grown by W. Kunnmann using techniques discussed in Ref. 6, p. 55.

11. J. S. Kouvel, Technical Report 210, Cruft Laboratory, Harvard University, (1 February 1955), unpublished.

12. $J_{AB}/kT_M = [SS_A(S_A + 1) S_B(S_B + 1)]^{-1} [3u/8 + \sqrt{2 + (3u/8)^2}].$

13. R. K. Wangsness, Phys. Rev. 97, 831 (1955).

14. P. B. Braun, Nature 170, 1123 (1952).

15. J. A. Schulkes and G. Blasse, J. Phys. Chem. Solids 24, 1651 (1963).

16. G. Blasse, J. Inorg. Nuclear Chem. 25, 743 (1963).

17. D. B. Rogers, R. J. Arnott, A. Wold, and J. B. Goodenough, J. Phys. Chem. Solids 24, 347 (1963).

18. J. L. Andrieux and H. Bozon, Compt. rend. 228, 565 (1949).

DOCUMENT CONTROL DATA - R&D

(Security classification of title, body of abstract and indexing annotation must be entered when the overall report is classified)

1. ORIGINATING ACTIVITY *(Corporate author)*	2a. REPORT SECURITY CLASSIFICATION
Lincoln Labs., Lexington, Mass.	UNCLASSIFIED
	2b. GROUP N/A

3. REPORT TITLE

Solid State Research

4. DESCRIPTIVE NOTES *(Type of report and inclusive dates)*

5. AUTHOR(S) *(Last name, first name, initial)*

6. REPORT DATE	7a. TOTAL NO. OF PAGES	7b. NO. OF REFS
Jun 64	75	18

8a. CONTRACT OR GRANT NO.	9a. ORIGINATOR'S REPORT NUMBER(S)
AF19(628)500	
b. PROJECT NO.	
c.	9b. OTHER REPORT NO(S) *(Any other numbers that may be assigned this report)*
d.	ESD-TDR-64-48

10. AVAILABILITY/LIMITATION NOTICES

Qualified Requesters May Obtain Copies From DDC.

11. SUPPLEMENTARY NOTES	12. SPONSORING MILITARY ACTIVITY
	ESD, L.G. Hanscom Field, Bedford, Mass.

13. ABSTRACT

This report summarizes the research and development efforts of the Solid State Division for the period 15 April to 15 July 1964. The Division devotes the majority of its activities to Solid State Device Research, Laser Research, Materials Research, Band Structure and the Spectroscopy of Solids and Magnetism and Resonance.

DD FORM 1473
1 JAN 64

14.		LINK A		LINK B		LINK C	
KEY WORDS		ROLE	WT	ROLE	WT	ROLE	WT
Solid State Research Laser Device Materials Magnetism radiation							

INSTRUCTIONS

1. ORIGINATING ACTIVITY: Enter the name and address of the contractor, subcontractor, grantee, Department of Defense activity or other organization (corporate author) issuing the report.

2a. REPORT SECURITY CLASSIFICATION: Enter the overall security classification of the report. Indicate whether "Restricted Data" is included. Marking is to be in accordance with appropriate security regulations.

2b. GROUP: Automatic downgrading is specified in DoD Directive 5200.10 and Armed Forces Industrial Manual. Enter the group number. Also, when applicable, show that optional markings have been used for Group 3 and Group 4 as authorized.

3. REPORT TITLE: Enter the complete report title in all capital letters. Titles in all cases should be unclassified. If a meaningful title cannot be selected without classification, show title classification in all capitals in parenthesis immediately following the title.

4. DESCRIPTIVE NOTES: If appropriate, enter the type of report, e.g., interim, progress, summary, annual, or final. Give the inclusive dates when a specific reporting period is covered.

5. AUTHOR(S): Enter the name(s) of author(s) as shown on or in the report. Enter last name, first name, middle initial. If military, show rank and branch of service. The name of the principal author is an absolute minimum requirement.

6. REPORT DATE: Enter the date of the report as day, month, year; or month, year. If more than one date appears on the report, use date of publication.

7a. TOTAL NUMBER OF PAGES: The total page count should follow normal pagination procedures, i.e., enter the number of pages containing information.

7b. NUMBER OF REFERENCES: Enter the total number of references cited in the report.

8a. CONTRACT OR GRANT NUMBER: If appropriate, enter the applicable number of the contract or grant under which the report was written.

8b, 8c, & 8d. PROJECT NUMBER: Enter the appropriate military department identification, such as project number, subproject number, system numbers, task number, etc.

9a. ORIGINATOR'S REPORT NUMBER(S): Enter the official report number by which the document will be identified and controlled by the originating activity. This number must be unique to this report.

9b. OTHER REPORT NUMBER(S): If the report has been assigned any other report numbers (either by the originator or by the sponsor), also enter this number(s).

10. AVAILABILITY/LIMITATION NOTICES: Enter any limitations on further dissemination of the report, other than those imposed by security classification, using standard statements such as:

(1) "Qualified requesters may obtain copies of this report from DDC."

(2) "Foreign announcement and dissemination of this report by DDC is not authorized."

(3) "U. S. Government agencies may obtain copies of this report directly from DDC. Other qualified DDC users shall request through

_____ ."

(4) "U. S. military agencies may obtain copies of this report directly from DDC. Other qualified users shall request through

_____ ."

(5) "All distribution of this report is controlled. Qualified DDC users shall request through

_____ ."

If the report has been furnished to the Office of Technical Services, Department of Commerce, for sale to the public, indicate this fact and enter the price, if known.

11. SUPPLEMENTARY NOTES: Use for additional explanatory notes.

12. SPONSORING MILITARY ACTIVITY: Enter the name of the departmental project office or laboratory sponsoring (paying for) the research and development. Include address.

13. ABSTRACT: Enter an abstract giving a brief and factual summary of the document indicative of the report, even though it may also appear elsewhere in the body of the technical report. If additional space is required, a continuation sheet shall be attached.

It is highly desirable that the abstract of classified reports be unclassified. Each paragraph of the abstract shall end with an indication of the military security classification of the information in the paragraph, represented as (TS), (S), (C), or (U).

There is no limitation on the length of the abstract. However, the suggested length is from 150 to 225 words.

14. KEY WORDS: Key words are technically meaningful terms or short phrases that characterize a report and may be used as index entries for cataloging the report. Key words must be selected so that no security classification is required. Identifiers, such as equipment model designation, trade name, military project code name, geographic location, may be used as key words but will be followed by an indication of technical context. The assignment of links, rules, and weights is optional